ADVANCED OPTICAL MICROSCOPY FOR THREE-DIMENSIONAL DEFORMATION, PROFILE AND TOMOGRAPHY MEASUREMENT

A Thesis

Presented to

The Academic Faculty

By

Zhipeng Pan

In Partial Fulfilment

of the Requirements for the Degree

Master of Science in the

George W. Woodruff School of Mechanical Engineering

Georgia Institute of Technology

May, 2016

ADVANCED OPTICAL MICROSCOPY FOR THREE-DIMENSIONAL DEFORMATION, PROFILE AND TOMOGRAPHY MEASUREMENT

Approved by:

Dr. Shuman Xia, Advisor
George W. Woodruff School of
Mechanical Engineering
Georgia Institute of Technology

Dr. Min Zhou
George W. Woodruff School of
Mechanical Engineering
Georgia Institute of Technology

Dr. Lei Zhu
George W. Woodruff School of
Mechanical Engineering
Georgia Institute of Technology

Date Approved: May 7, 2015

ACKNOWLEDGEMENTS

I would like thank to my advisor, Professor Shuman Xia, for his support and guidance throughout these two years. He showed me lots of his hands on experiences on setting up experiment, analyzing data and paper writing. It's my great pleasure working with him. I would like to thank him again for his support and supervising.

I also want to thank my committee member Prof. Min Zhou and Prof. Lei Zhu. The kind suggestions and generous idea helped me a lot in working on the thesis. The insight and general knowledge greatly improved the quality of my research work.

In addition, I want to thank my lab mates, Xueju, Neng and Noah, for their kind help. I enjoyed a great time working with them at Georgia Tech.

Last but not least, I want to thank my mom, daddy, brother and my girlfriend Chong, for their continuous support and encouragement during my study.

TABLE OF CONTENTS

LIST OF TABLES

LIST OF FIGURES

SUMMARY

A diffraction assisted image correlation (DAIC) method is proposed for three-dimensional (3D) deformation measurement, surface profiling, and tomographic reconstruction. We show that, through a pinhole projection model, the 3D shape and deformation of an object can be measured by performing two-dimensional digital image correlation analysis between the two first-order diffracted views. A fluorescent 3D microscope with sub-micron spatial resolution and sub-pixel measurement accuracy is developed based on the DAIC method. To extend the depth of focus of the 3D microscope, a diffraction assisted light field microscopy is developed by inserting a microlens array in the microscope's imaging path. The capability of the 3D microscope for tomographic reconstruction with improved axial resolution is demonstrated.

CHAPTER 1

INTRODUCTION

1.1 Motivation

Three-dimensional (3D) measurement technique is playing increasingly prominent roles in both scientific research and industrial application [1], such as materials deformation characterization [2], 3D medical imaging [3], robotic control [4] and geometry checking of mechanical parts [5]. The recent development of digital imaging devices, laser scanning techniques and other light sensor devices combined with digital signal processing, enables the fast development of 3D measurement techniques. Compared with stylus based microscope and electron beam microscope, optical 3D measurement methods provide many advantages such as low costs, biocompatibility and fast sampling speed.

Based on the sampling method, existing 3D optical measurement methods can be divided into two main categories: spatial-scanning method and full-field method [6]. The first category includes time-of-flight (TOF) depth profiling, scanning-laser confocal microscopy, chromatic depth scanning method, and triangulation-based laser spot scanning or line scanning approaches. All of these methods are intrinsically point-wise or line-wise scanning methods, but can achieve full-field measurement by means of spatial scanning. In the second category of inherent full-field techniques, 3D perception is usually achieved by digital processing of a sequence of two-dimensional coherent or incoherent optical images. Some of the commonly used full-field methods include white light and laser interferometry, projection Moire interferometry, depth from focus/defocus

(DFF/DFD), as well as 3D digital image correlation (3D-DIC). In general, the full-field methods allow much faster 3D measurement than the spatial-scanning methods.

Digital image correlation (DIC) has been established as an effective tool for full-field motion, shape and deformation measurement with high accuracy at various length scales ranging from landscape profiling and micro electronic devices deformation measurement [7-9]. Stereo-imaging system has been implemented with DIC for 3D shape and deformation measurement from millimeter to meter scale [10, 11]. When the length scale comes down to the micrometer range, shallow depth of focus and accurate calibration of the multi-camera system pose great challenges for the implementation.

In this thesis, a novel diffraction assisted image correlation method (DAIC) method is developed to allow a single camera imaging system for 3D profile, deformation and tomography measurement. The DAIC method combines a transmission diffraction grating with two dimensional digital image correlation (2D-DIC) method by inserting a transmission diffraction grating between the camera and the imaging target. We exploit the light splitting and shifting characteristics of the transmission grating to obtain the three-dimensional information of the imaging target. The distortion due the camera and the transmission diffraction grating is calibrated and its influence on the measurement accuracy has been investigated. Taking advantage of the high accuracy and simplicity for implementation, a compact optical 3D microscope is developed that is able to measure submicron scale displacement and surface profile.

The recently developed light field microscope is capable of reconstructing the volumetric data of a specimen with extended depth of field in a single shot [12, 13]. But the performance of the system is greatly constrained by its poor axial resolution. In the

current study, we integrate our 3D microscopy with the light field technique to enable 3D high-resolution tomographic reconstruction. We show that, by inserting a diffraction grating between the imaging specimen and the objective lens, two first-order diffracted light field images could be formed in the camera sensor plane for tomographic reconstruction. The axial resolution of reconstructed 3D stacks is found to be greatly improved by a diffraction assisted light field rendering method without sacrificing the lateral resolution.

1.2 Outline of the Thesis

Chapter 2 will first introduce the DAIC method for macroscopic 3D shape and displacement measurement. The basic theory of the DAIC method will be presented in detail. Validation test results on a Barbie doll's face and a set of well-defined cylindrical, conical and step surfaces will be presented to illustrate the implementation and performance of the proposed method. The error analysis of the DAIC method from the lens distortion and transmission grating distortion will also be discussed.

In Chapter 3, a compact, high-accuracy 3D microscope that is capable of measuring 3D displacement and deformation at the microscopic scale will be reported. The microscope system is based on a seamless integration of the DAIC method with fluorescent microscopy. We will experimentally demonstrate the microscope's capability for 3D measurements with submicrometer spatial resolution and subpixel measurement accuracy. Potential applications and limitation of the microscope will be discussed at the end of the chapter 3.

To overcome the shallow depth of focus problem of the 3D microscope, we have combined the light field imaging technique with the DAIC method. In chapter 4, a diffraction assisted light field microscope (DLFM) for 3D tomographic reconstruction with improved axial resolution will be reported.

CHAPTER 2

DIFFRACTION ASSISTED IMAGE CORRELATION FOR THREE-DIMENSIONAL SURFACE PROFILING

2.1 Introduction

High-fidelity, full-field reconstruction of three-dimensional (3D) surfaces is playing increasingly prominent roles in materials [14, 15] and biological research [16], 3D scanning [6, 17], and automated inspection [18, 19]. Compared to conventional stylus-based surface profiling techniques, optical-based profiling methods offer many unique advantages, such as non-contact/non-intrusive measurement capability, fast sampling speed, and wide measurement range.

Existing optical methodologies for topographical characterizations can be divided into two main categories: spatial-scanning methods and one-shot acquisition methods. The first category includes time-of-flight (TOF) depth profiling [20], scanning-laser confocal microscopy [21-23], chromatic depth scanning method [24], and triangulation-based laser spot scanning or line scanning approaches [25]. All of these methods are intrinsically point-wise or line-wise scanning methods, but can achieve full-field measurement by means of spatial scanning. In the second category of inherent full-field techniques, topographic reconstruction is usually achieved by digital processing of a sequence of two-dimensional coherent or incoherent optical images. Some of the commonly used full-field methods include white light and laser interferometry [15, 26-28], projection Moire interferometry [29], depth from focus/defocus (DFF/DFD) [30-32], as well as 3D digital image correlation (3D-DIC) [33-35]. In general, the one-shot

acquisition methods allow much faster 3D topographic construction than the spatial-scanning methods.

Recently, Xia et al. [36] developed a novel image correlation-based technique named Diffraction-Assisted Image Correlation (DAIC) for 3D deformation measurement. The DAIC method involves viewing a test specimen under monochromatic illumination through a transmission diffraction line grating. The grating produces multiple diffracted face views of the specimen that are free from perspective distortion. The apparent in-plane displacements of the positive and negative first-order diffracted views are obtained through two-dimensional digital image correlation (2D-DIC) analysis, and algebraically manipulated to determine the 3D displacement of the specimen. Motivated by this work, a diffraction-assisted grid method was recently developed by Notbohm et al. [37], who combined the 2D grid method [38-40] and the use of a diffraction grating to achieve 3D measurement.

In the present study, we extend the original DAIC method for 3D surface profile measurement. We show that, without major modification to the DAIC setup previously developed for 3D displacement measurement, 3D topographical reconstruction can be readily achieved by performing 2D correlation analysis between the two diffracted views of different diffraction orders. This new surface profiling method eliminates the need for stereoscopic imaging as required by classical 3D-DIC, thus resulting in a compact and simple setup that is more suitable for dynamic and microscopic measurement of small objects. Furthermore, the use of 2D correlation and algebraic operations for 3D shape measurement significantly reduces the computational effort as compared with traditional stereo-vision based methods.

2.2 Theory

When a single camera is used to directly view a curved object surface, the depth information of the object is lost during 2D image projection. The proposed profiling approach involves placing a transmission line grating in the imaging path to create a 3D perception, as shown in Fig. 1. Due to first-order light diffraction by the grating, two virtual objects are formed on both sides of the real object. Consider a point (*P*) on the real object surface at a height of *h*, measured from a fixed reference plane parallel to the grating surface and near the object surface. The two corresponding virtual points (P^+ and P^-) are located at a distance of $d^{\pm} = (d-h)/\cos^3\theta$ from the grating [36]. Here *d* is the distance between the grating and the reference plane, $\theta = \sin^{-1}(\lambda/p)$ is the first-order diffraction angle, λ is the wavelength of the light source, and *p* is the pitch of the grating. The position vectors of P^+ and P^-, $\mathbf{X}_{P^{\pm}}$, are related to the position vector of *P*, $\mathbf{X}_P$, via the equation

$$\mathbf{X}_{P^{\pm}} = \mathbf{X}_P - (d-h)\left(\frac{1}{\cos^3\theta} - 1\right)\mathbf{i}_{\mathrm{n}} \pm (d-h)\tan\theta\,\mathbf{i}_{\perp}, \tag{2.1}$$

in which $\mathbf{i}_{\mathrm{n}}$ is an out-of-plane unit vector normal to the grating surface, and $\mathbf{i}_{\perp}$ is an in-plane unit vector perpendicular to the grating rulings.

Assuming a pinhole camera model, P^+ and P^- are projected to I^+ and I^- in the image plane of the camera, as shown in Fig. 1. The position vectors of the two image points in the unit of pixels, $\mathbf{X}_{I^{\pm}}$, are related to $\mathbf{X}_{P^{\pm}}$ according to

$$\mathbf{X}_{I^{\pm}} = \mathbf{X}_{P^{\pm}} \frac{f/b}{s + [(d-h)/\cos^3\theta]} + \mathbf{e}_{I^{\pm}}, \tag{2.2}$$

where b is the physical pixel size of the imaging sensor, s is the distance between the

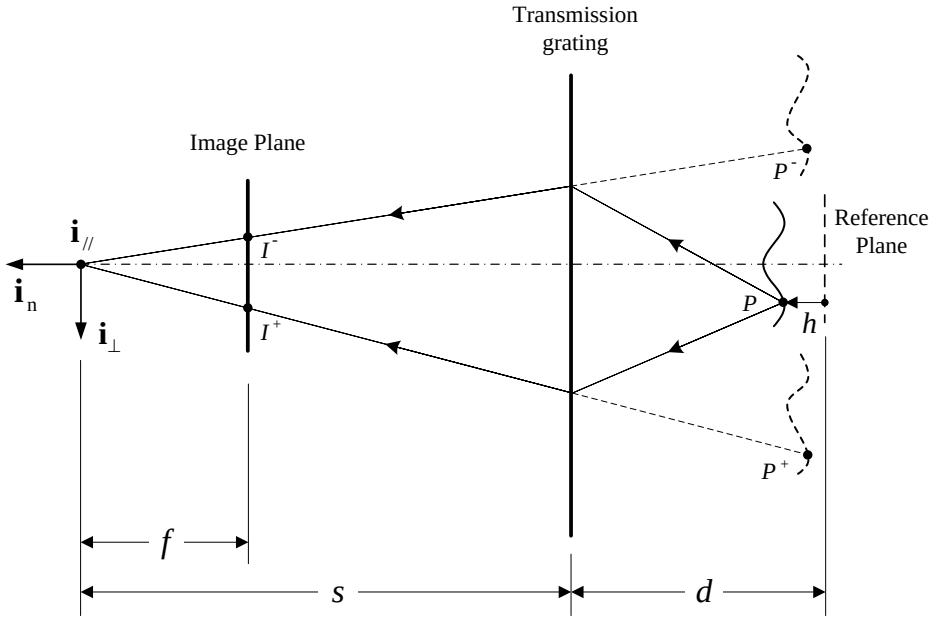

Figure 1. Optical arrangement for 3D profile measurement by the diffraction-assisted image correlation (DAIC) method. $\mathbf{i}_\perp$ and $\mathbf{i}_{//}$ are unit vectors perpendicular and parallel to the grating rulings, respectively, and $\mathbf{i}_n$ is a unit vector normal to the grating surface.

pinhole and the grating, f is the distance between the pinhole and the image plane in physical unit, and $\mathbf{e}_{I^\pm}$ are the projection errors associated with camera/lens/grating distortion. In the classical pinhole camera model, there are four intrinsic camera parameters: (f_x, f_y, c_x, c_y). f_x and f_y are the focal distances expressed in units of horizontal and vertical pixels, and c_x and c_y are the coordinates of the principal point in units of horizontal and vertical pixels. In this work, we consider square-shaped pixels and therefore the numerator (f/b) in Eq. (2) is equal to f_x and f_y. Note that c_x and c_y do not show up in Eq. (2.2) because the position vectors of the virtual points and the image

points ($\mathbf{X}_{P^{\pm}}$ and $\mathbf{X}_{I^{\pm}}$) are both expressed in a rectangular coordinate system with its origin placed at the pinhole. Substitution of Eq. (2.1) into Eq. (2.2) and computation of the in-plane components of $\mathbf{X}_{I^{\pm}}$ yield

$$\mathbf{X}_{I^{\pm}}^{\mathbf{In-plane}} = [\mathbf{X}_{P}^{\mathbf{In-plane}} \pm (d-h)\tan\theta\,\mathbf{i}_{\perp}]\frac{f/b}{s+[(d-h)/\cos^3\theta]} + \mathbf{e}_{I^{\pm}}. \tag{2.3}$$

The above equation can be linearized by assuming the surface height is much smaller than the camera-object distance (i.e., $h << s\cos^3\theta + d$). The linearization results in the following two expressions

$$\mathbf{X}_{I^{+}}^{\mathbf{In-plane}} = [\mathbf{X}_{P}^{\mathbf{In-plane}} + \frac{h}{s\cos^3\theta + d}\mathbf{X}_{P}^{\mathbf{In-plane}} - (\frac{s\cos^3\theta}{s\cos^3\theta + d}h - d)\tan\theta\,\mathbf{i}_{\perp}]\frac{1}{b'} + \mathbf{e}_{I^{+}}, \tag{2.4a}$$

$$\mathbf{X}_{I^{-}}^{\mathbf{In-plane}} = [\mathbf{X}_{P}^{\mathbf{In-plane}} + \frac{h}{s\cos^3\theta + d}\mathbf{X}_{P}^{\mathbf{In-plane}} + (\frac{s\cos^3\theta}{s\cos^3\theta + d}h - d)\tan\theta\,\mathbf{i}_{\perp}]\frac{1}{b'} + \mathbf{e}_{I^{-}}, \tag{2.4b}$$

where $b' = [s + (d/\cos^3\theta)]b/f$ is the projected pixel size in the object plane.

By subtracting Eqs. (2.4a) and (2.4b), we obtain the following equation for determining the surface height profile:

$$h = \left\{ d - \frac{b'}{2\tan\theta}[\mathbf{u}_{I}^{\mathbf{In-plane}} - (\mathbf{e}_{I^{+}} - \mathbf{e}_{I^{-}})]\cdot\mathbf{i}_{\perp} \right\}(1 + \frac{d}{s\cos^3\theta}). \tag{2.5}$$

$\mathbf{u}_{I}^{\mathbf{In-plane}} = \mathbf{X}_{I^{+}}^{\mathbf{In-plane}} - \mathbf{X}_{I^{-}}^{\mathbf{In-plane}}$ in the above equation is the in-plane displacement from I^{-} to I^{+} which can be determined by performing a 2D image correlation analysis. Note that the field of $\mathbf{u}_{I}^{\mathbf{In-plane}}$ obtained by image correlation (and therefore *h* given by Eq. (2.5)) is expressed in the reference configuration, i.e., the coordinate space of $\mathbf{X}_{I^{-}}^{\mathbf{In-plane}}$. To map $\mathbf{X}_{I^{-}}^{\mathbf{In-plane}}$ to the object coordinate space, we add Eqs. (2.4a) and (2.4b) to get

$$\mathbf{X}_P^{\mathbf{In-plane}} = \left\{ \mathbf{X}_{I^-}^{\mathbf{In-plane}} + \frac{\mathbf{u}_I^{\mathbf{In-plane}} - (\mathbf{e}_{I^+} + \mathbf{e}_{I^-})}{2} \right\} b'(1 + \frac{h}{s\cos^3\theta + d})^{-1}. \quad (2.6)$$

The distributions of $h(\mathbf{X}_{I^-}^{\mathbf{In-plane}})$ and $\mathbf{X}_P^{\mathbf{In-plane}}(\mathbf{X}_{I^-}^{\mathbf{In-plane}})$ obtained using Eqs. (2.5) and (2.6) can then be combined to yield the height profile as a function of planar object coordinates, $h(\mathbf{X}_P^{\mathbf{In-plane}})$.

If we choose a sensor (image) coordinate system (x, y) with its y-axis parallel to the grating grooves, the object height profile given by Eq. (2.5) can be rewritten as

$$h(x, y) = \left\{ d - \frac{u_x(x, y) - [e_x(x + u_x, y) - e_x(x, y)]b'}{2\tan\theta} \right\} (1 + \frac{d}{s\cos^3\theta}), \quad (2.7a)$$

and the planar object coordinates become

$$x_p(x, y) = \left\{ x + \frac{u_x(x, y) - [e_x(x + u_x, y) + e_x(x, y)]}{2} \right\} b'(1 + \frac{h(x, y)}{s\cos^3\theta + d})^{-1}, \quad (2.7b)$$

$$y_p(x, y) = \left\{ y + \frac{u_y(x, y) - [e_y(x + u_x, y) + e_y(x, y)]}{2} \right\} b'(1 + \frac{h(x, y)}{s\cos^3\theta + d})^{-1}, \quad (2.7c)$$

in which $u_x(x, y)$ and $u_y(x, y)$ denote the x- and y-displacement fields between the negative and positive first-order images, and e_x and e_y are the geometric image distortions in the x- and y-directions.

2.3 Experimental

2.3.1 *Experimental Setup*

An experimental realization of the proposed surface profiling method is shown in Fig. 2. A digital camera (DFK 72AUC02, Imaging Source, Charlotte, NC) equipped with a 35 mm focal length lens (HF35HA-1B, Fujinon, Stamford, CT) was used for image acquisition. The camera had an 8-bit, 2592×1944 pixel CMOS sensor with a square pixel size of 2.2 μm. A pair of blazed transmission gratings (GT25-03, Thorlabs, Newton, NJ)

with 300 lines/mm groove density was placed between the lens and a test specimen, to

(a)

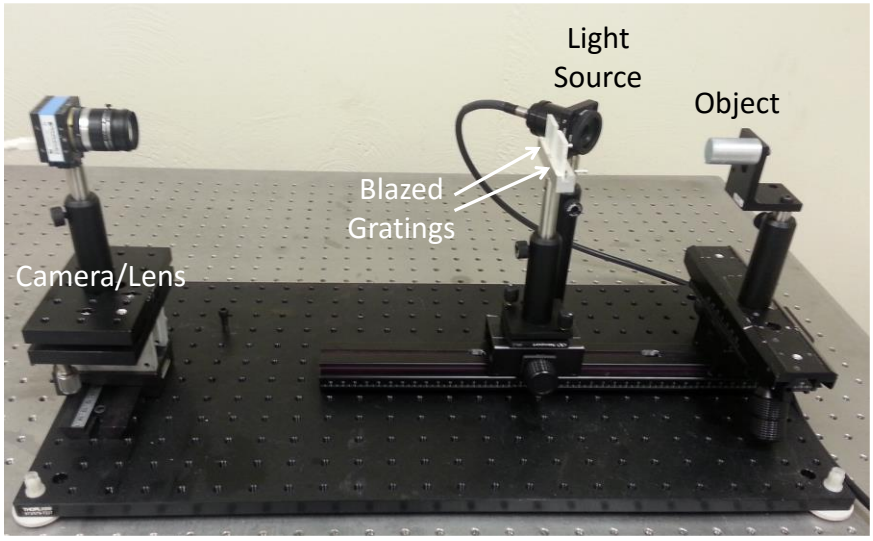

(b)

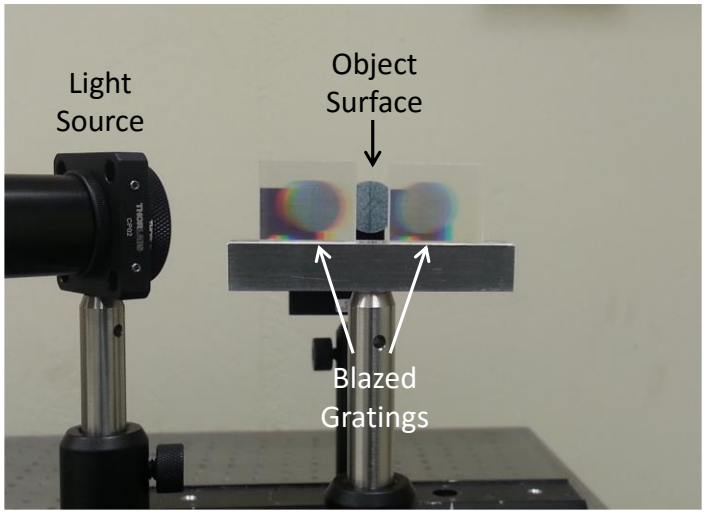

Figure 2. (a) Experimental setup of the proposed surface profiling method; (b) front view of the gratings and the object surface taken under ambient room lighting. Note that the two diffracted views are blurred due to chromatic dispersion of the gratings, necessitating the use of monochromatic illumination for accurate surface profile measurement.

produce positive and negative first-order diffracted views of the specimen. The gratings had a dimension of 25×25 mm, limiting the largest possible measurement area to about the same size. A light-emitting diode (LED) light source was used with a narrow-band optical filter (632-634 nm band pass, FL05632.8-1632, Thorlabs, Newton, NJ) to provide even quasi-monochromatic illumination. In all experiments, the distance between the gratings and the optical center of the lens was fixed at 307 mm. The lens was focused at a reference plane 109 mm behind the gratings and had a depth-of-field of ±4 mm. The specimen surface was positioned within 2 mm of the reference plane for surface profiling. There were a few factors involved to set up the geometry of our experiment. The distance between the camera and the specimen was determined by the working distance and field-of-view of the imaging lens. The grating-specimen distance was proportional to the spacing between the two diffracted views. Therefore, this distance needed to be sufficiently large to avoid overlapping of the diffracted views.

The surface to be measured was first spray-painted with white paint as background, and then speckle patterned with green paint to enable image correlation. A DIC analysis was performed between the two diffracted views using the VIC-2D software (Correlated Solutions, Inc., W. Columbia, SC) with a subset size of 59×59 pixels and a step size of 5 pixels. The correlated displacement field was then used to compute a surface height map of the specimen according to Eqs. (2.7a)-(2.7c).

2.3.2 Image Distortion Calibration

As can be seen from Eqs. (2.7a)-(2.7c), the geometric image distortion affects the determination of both height profile and planar coordinates in an additive manner, and needs to be corrected for the sake of accuracy. The distortion in the DAIC optical system

has three possible components: image distortion due to grating imperfection, lens distortion, and distortion caused by non-uniform spatial distribution of the sensing pixels (thereafter referred to as the sensor distortion). Our previous study showed that the first type of distortion is negligible for the transmission gratings used [36]. The lens distortion is usually well described by Brown's model [41] in which the radial and tangential distortion components are expressed as polynomial functions of image coordinates. The coefficients of these polynomials can be determined through calibration against a precision test target. The sensor distortion is related to the manufacturing tolerances and techniques of image sensors and does not obey a simple parametric distribution. This type of distortion has generally been overlooked in previous work, but as we will show, it plays an important role in the present study.

We adopt a non-parametric method of distortion calibration developed by Yoneyama et al. [42], to determine the combined lens and sensor distortion in our optical system. In this method, a rectangular grid pattern is aligned with the principal image axes, and a single image of the grid pattern is acquired and analyzed with a Fourier transform-based algorithm. The analysis yields the phase maps, δ_x and δ_y, of the grid pattern, which are related to the *x*- and *y*-directional image distortions through

$$e_x = \frac{\delta_x}{2\pi} p_{x0},\ e_y = \frac{\delta_y}{2\pi} p_{y0}, \tag{2.8}$$

where p_{x0} and p_{y0} are the *x*- and *y*-directional pitches of the grid pattern. In our calibration experiment, we chose a high-precision Ronchi line grating (56-619, Edmund Optics, Barrington, NJ) with a pitch of 0.254 mm (~ 10 pixels), as opposed to the grid pattern used in the original method. This choice was made because of non-availability of

a high-precision grid target of desired pitch. The *x*- and *y*-directional distortion distributions were measured separately by aligning the grating's groove direction with the *x*- or *y*-direction of the image plane. The alignment was carefully done by adjusting the angular position of the grating with a tilt stage and aligning the visible grating lines with the *x*- or *y*-axis of the display screen.

2.4 Results

The proposed profiling method was first applied to topographic reconstruction of a Barbie doll's face to test its validity. The positive first (+1) order and negative first (-1) order images of the Barbie doll's face seen through the pair of blazed gratings are shown in Fig. 3(a) and (b). The two speckle images were correlated using the VIC-2D software to obtain the apparent in-plane displacement field. Neglecting any geometric distortion in the images, this displacement field was used in Eqs. (2.7a)-(2.7c) to construct a surface profile map as shown in Fig. 3(c). The characteristic facial features, such as the forehead, nose and lips, are clearly discernible in the contour map, thereby qualitatively validating the proposed method.

To quantitatively assess the measurement accuracy that can be achieved by the DAIC method, we carried out 3D shape measurement on a set of well-defined surfaces which were prepared by machining with a precision of 2.5 μm. The surfaces used included a cylindrical surface with a radius of 36.00 mm, a conical surface with a half-apex angle of 76.16^{o}, and a 1.46 mm step height. These surface types were chosen to investigate the effect of different orders of surface continuity on the measurement accuracy; the cylindrical surface was smooth and infinitely differentiable; the conical surface was

continuous but not differentiable at the apex; the step height had an abrupt line of discontinuity.

(a) 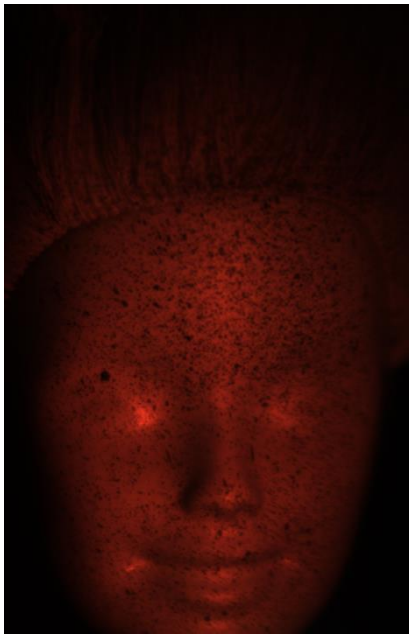

-1^{st} order

(b) 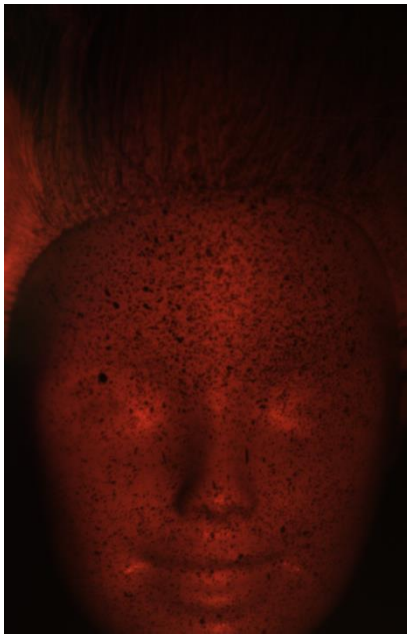

$+1^{st}$ order

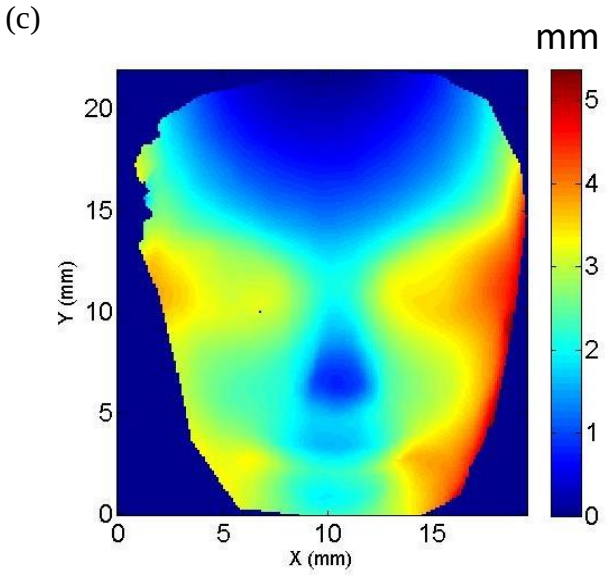

Figure 3. (a) Speckle images of the (a) negative and (b) positive first-order diffracted views of a Barbie doll's face; (c) measured topographic map of the Barbie doll's face.

The measured height contour plots of the three surfaces without image distortion correction are presented in Fig. 4. The height profiles along the dashed lines in Fig. 4 are plotted in Fig. 5(a)-(c), together with the true surface profiles calculated from the surface parameters. Each measured profile is registered with the corresponding true profile by translating and rotating the measured profile to minimize the square sum of the errors. The reconstructed shapes are found to match well with their true counterparts. A more stringent comparison is shown in Fig. 5(d)-(f), where the difference between the experimental and true profiles is plotted for each surface. The error in the measured cylindrical surface profile is small near the center of the surface, and increases to ~0.04 mm towards the both ends. The measured height profiles of the conical and step surfaces have significant errors at the centers where a discontinuity occurs. These large errors are caused by the inherent smoothing nature of the image correlation algorithm used. Apart from the discontinuities, lower error profiles similar to that found for the smooth

cylindrical surface are seen. This similarity suggests that systematic errors due to image distortion are present in the three reconstructed shapes and may be ruled out through careful distortion compensation.

The calibration approach explained in Section 2.3.2 was applied to correct the errors due to optical distortion. Fig. 6 shows the calibrated distributions of image distortion along the *x*- and *y*-directions, $e_x(x, y)$ and $e_y(x, y)$, as well as the magnitude of distortion (calculated as $\sqrt{e_x^2 + e_y^2}$). The amount of distortion is small over the whole field (less than 0.2% of the field-of-view). It is noted that the three distortion patterns do not possess good symmetry or anti-symmetry as typically seen for lens distortion. Therefore, we conclude that the measured distortion is primarily attributed to the sensor distortion. With this distortion taken into account, the height profiles of the three surfaces were re-calculated by deducting the image distortion maps from the in-plane displacement maps according to Eqs. (2.7a)-(2.7c) and are displayed in Fig. 7. The root-mean-square (RMS) errors are reduced to 10 μm away from the discontinuities for all three surfaces, while the large errors at the discontinuities remain unaffected.

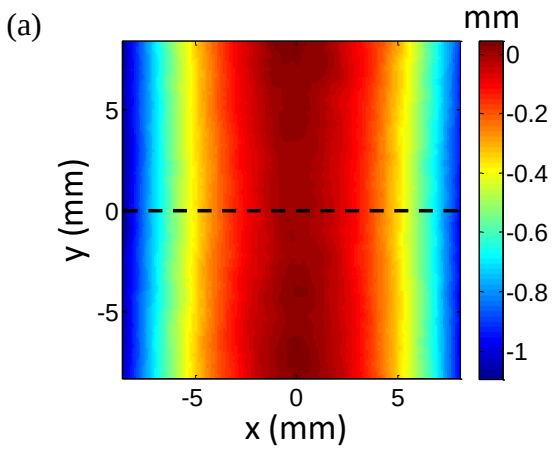

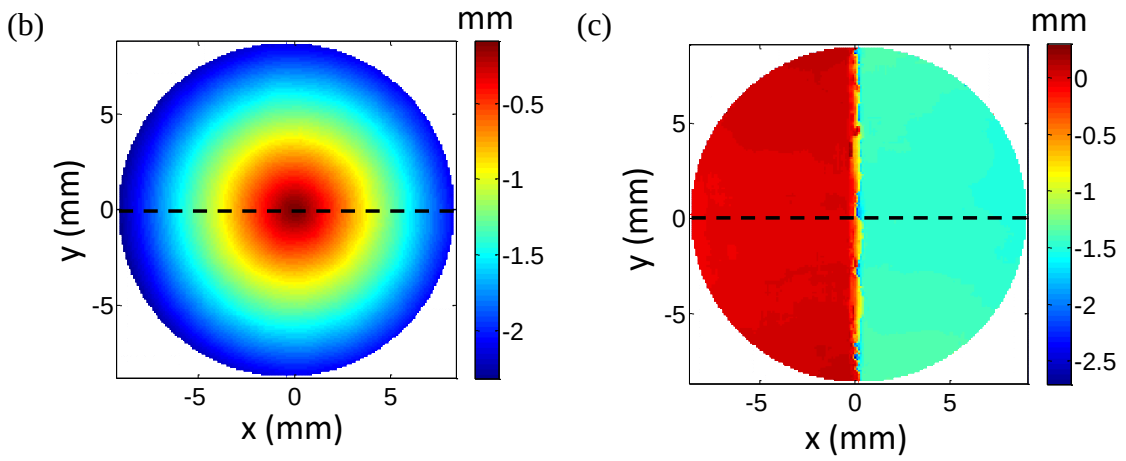

Figure 4. Measured surface height maps of (a) a cylindrical surface, (b) a conical surface, and (c) a step surface.

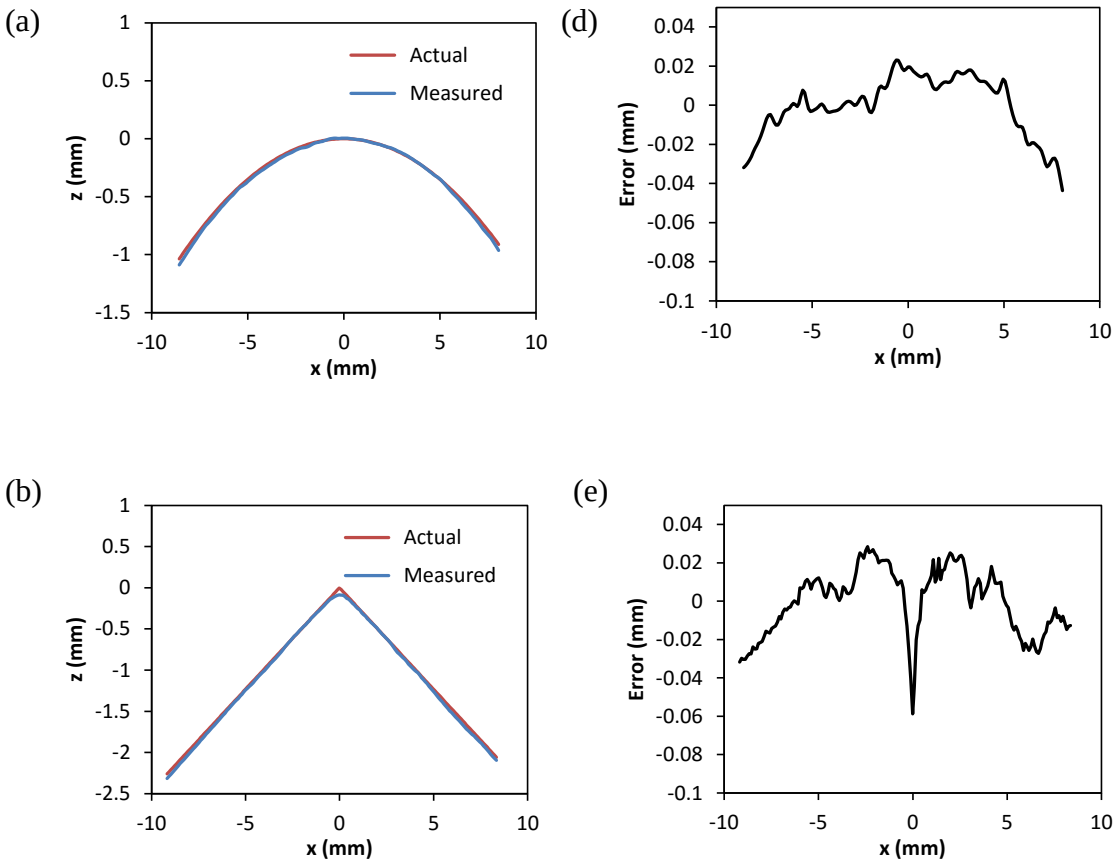

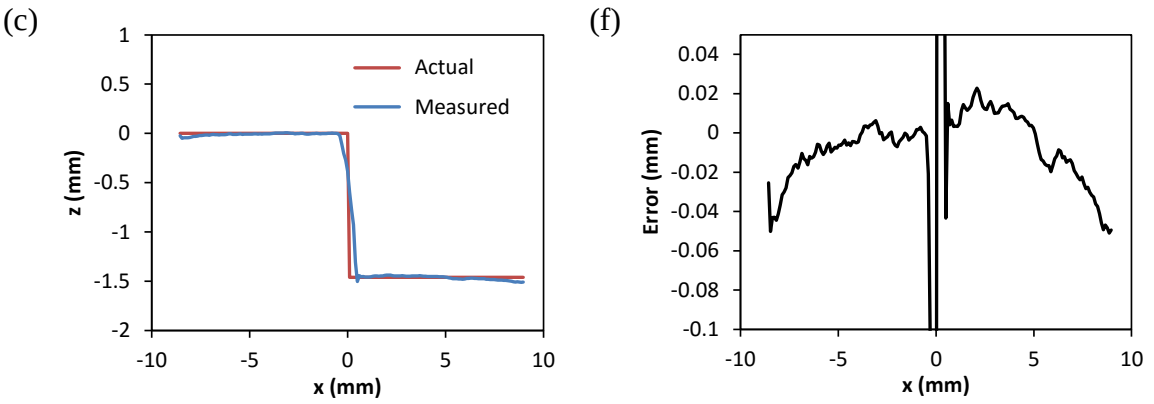

Figure 5. Comparison between the measured and true surface profiles along the dashed lines shown in Figure. 4 for (a) the cylindrical surface, (b) the conical surface, and (c) the step surface; measurement errors in the height profiles of (d) the cylindrical surface, (e) the conical surface, and (f) the step surface.

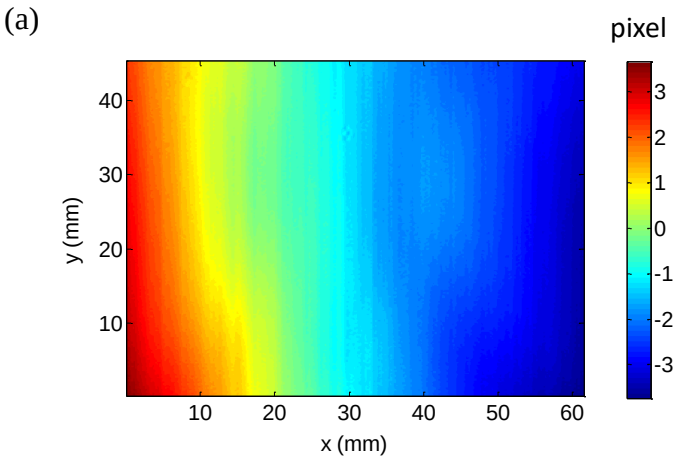

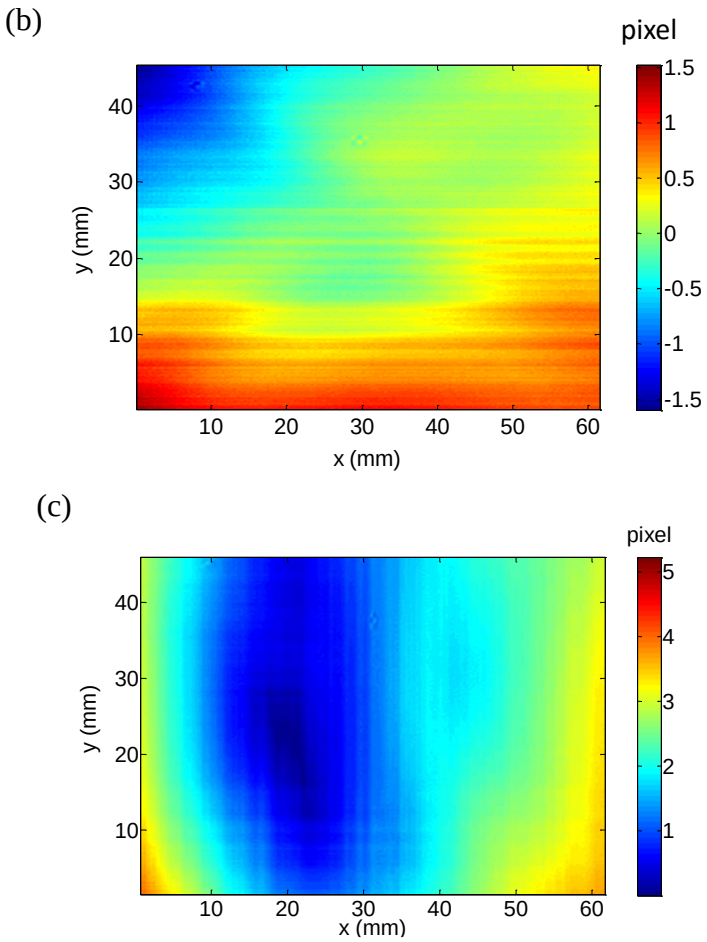

Figure 6. Calibrated image distortion distributions along the (a) x- and (b) y-directions; (c) magnitude of image distortion.

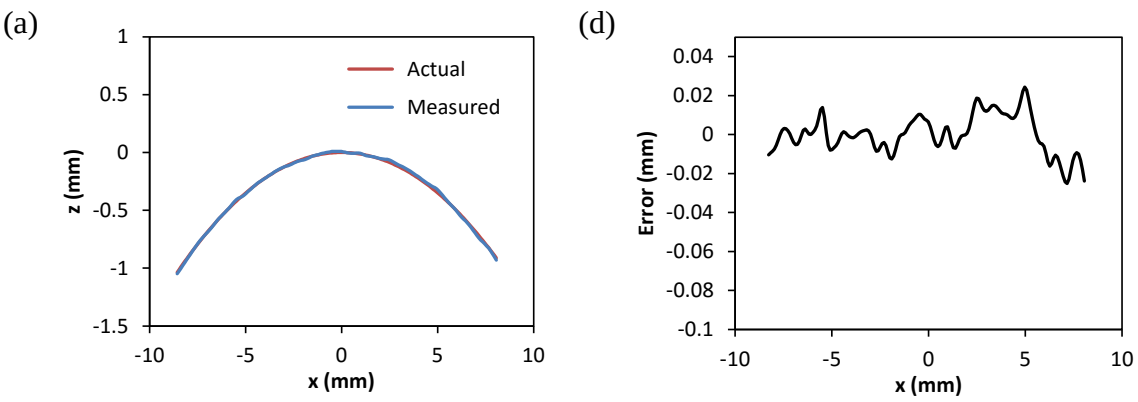

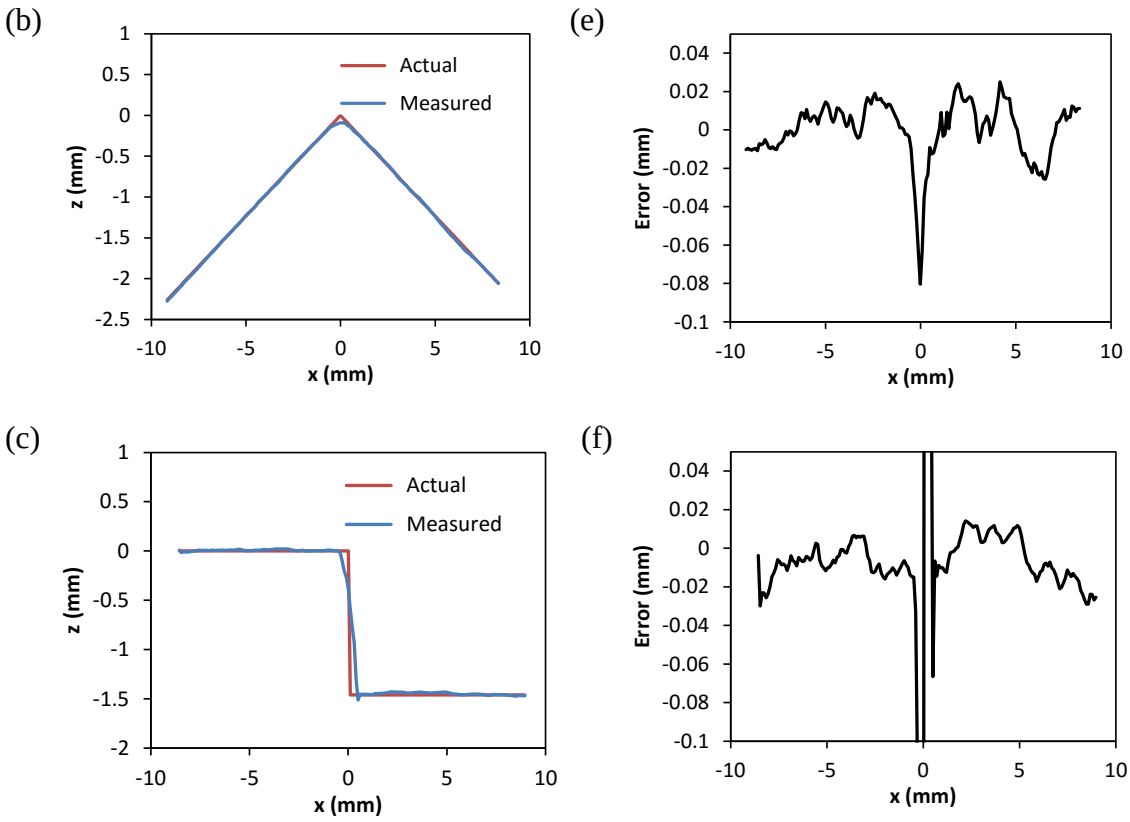

Figure 7. Comparison between the true and measured surface profiles after distortion compensation for (a) the cylindrical surface, (b) the conical surface, and (c) the step surface; measurement errors in the surface profiles after distortion compensation for (d) the cylindrical surface, (e) the conical surface, and (f) the step surface.

2.5 Discussion

There are four main sources of error associated with applying the DAIC method for 3D shape measurement. The first type of error is caused by uncertainty in determining the geometrical parameters of the optical setup. According to Eq. (2.7a), the relative measurement error in the surface profile can be estimated by error propagation as

$$\left(\frac{\varepsilon_h}{h}\right)^2 = \left(\frac{\varepsilon_u}{u}\right)^2 + \left[\left(\frac{\varepsilon_d}{d}\right)^2 + \left(\frac{\varepsilon_s}{s}\right)^2\right] \Big/ \left(1 + \frac{s\cos^3\theta}{d}\right)^2$$

(2.9)

in which u is the in-plane displacement and (ε_u, ε_s, ε_d) are the absolute measurement errors in (u, s, d). In the present study, s and d are determined to be 307 mm and 109 mm, respectively, with submillimeter accuracy. The in-plane displacement measurement has a relative error ($\frac{\varepsilon_u}{u}$) around 0.5%. Therefore, the contribution of ε_s and ε_d to the total error is estimated to be more than one order of magnitude lower than that of ε_u and is not considered as a major source of error. The second type of error is due to geometric image distortion. As demonstrated in the present study, this error can be fully corrected by distortion calibration and compensation. The third source of error comes from the uncertainty of displacement measurement by 2D-DIC. The image correlation error, ε_u, which is dependent on various factors, such as speckle pattern, subset shape function, subset size, and grayscale bit depth, is usually at a sub-pixel level. From Eq. (2.7a), the measurement error in the surface profile resulted from ε_u is

$$\varepsilon_h = \frac{\varepsilon_u b'}{2\tan\theta}\left(1 + \frac{d}{s\cos^3\theta}\right) \tag{2.10}$$

By performing DIC measurement of an in-plane rigid-body translation, we found the value of ε_u in the present study was about 0.09 pixel. According to Eq. (10), this value corresponds to a surface profile error of 7.9 μm, which compares well with the actual error of 10 μm observed in our experiments. Eq. (2.10) also suggests that a large first-order diffraction angle can help suppress the measurement error associated with ε_u.

The last type of measurement error occurs when the measured surface has a low order of continuity. Classical 2D-DIC algorithms are based on the correlation of a subset area between the reference and deformed images. The correlation analysis assumes a uniform deformation mode within the subset, making standard 2D-DIC unsuitable for measuring discontinuous displacement fields. Several attempts have been made recently to develop new image correlation algorithms that are capable of handling displacement discontinuities. Jin and Bruck [43] proposed a pointwise DIC method that allows the displacement of each pixel within a subset to be assessed independently. Réthoré et al. [44] applied the concept of the extended finite element method to image correlation analysis, and demonstrated the flexibility and accuracy of their scheme for measuring irregular displacement fields. More recently, Poissant et al. [45] made a direct extension to standard DIC by allowing a subset to be split when a discontinuity is detected. When the DAIC method is combined with one of these discontinuity-preserving DIC algorithms, we can expect a substantial improvement in accuracy for measuring discontinuous surfaces. The actual implementation of this idea, though, is not within the scope of this paper.

Spray-painting has been used in this work to produce affixed random speckle patterns as needed for image correlation analysis. Other less invasive patterning strategies (e.g., laser speckle patterning or digital patterning by a video projector) may be employed to facilitate correlation. It is also possible to use regular patterns instead of random patterns; in this case, alternative full-field displacement measurement techniques to 2D-DIC, such as the grid method [38-40] or the object grating method [46], can be assisted by the use of a diffraction grating to achieve 3D surface profiling.

The DAIC surface-profiling method utilizes a transmission grating and a single camera to achieve 3D perception, making it particularly suitable for dynamic and microscopic measurement. Coupled with a high-speed camera, the DAIC method can be readily adopted for dynamic 3D shape measurement. This arrangement overcomes the cost and synchronization issues commonly associated with existing stereo vision-based approaches using multiple cameras. It is also envisioned that the method presented here may be implemented in optical microscopy to enable multiscale topographic analysis. Nevertheless, we also recognize several limitations of our profiling method. First, a test object must be in full view through the transmission gratings used, thus limiting the maximum size of the object to the grating size. Large transmission gratings, such as holographic diffraction grating films up to 6×12 inches (54-509, Edmund Optics, Barrington, NJ), are now readily available at low cost. Therefore it is believed that the practical limit for measurable object sizes is on the order of tens of cm, even though larger object sizes may be achievable using custom-made gratings at the expense of increased cost. Second, monochromatic illumination is required in our method to prevent chromatic dispersion of the diffraction gratings. This entails the use of a speckle pattern with a good-contrast color that is matched to the illumination wavelength. Finally, the surface profile equations (Eqs. (2.5) and (2.7a)) are derived assuming that the grating surface is perpendicular to the optical axis of the camera. Future work could relax this assumption by considering a more versatile geometric configuration.

2.6 Conclusions

A new full-field optical method for surface profile measurement is presented. This method involves the use of a single camera and a transmission grating to achieve 3D perception and the application of 2D-DIC for rapid 3D shape reconstruction. The theoretical basis of the proposed method is provided by assuming a pinhole projection model and accounting for possible geometric image distortion. The validity and accuracy of the method have been demonstrated on a set of object surfaces with different levels of surface continuity. It is found that systematic measurement errors occur due to distortion from lens imperfection and non-uniform distribution of sensing pixels, but can be corrected with a non-parametric distortion-correction scheme. The proposed method is simple and easy to implement, and is advantageous over existing stereo-vision based ones for high-speed and microscopic 3D shape measurement of small objects.

CHAPTER 3

A NOVEL OPTICAL MICROSCOPE FOR MICROSCALE THREE DIMENSIONAL SURFACE DISPLACEMENT AND SHAPE MEASUREMENT

3.1 Introduction

3D full-field deformation and morphology analyses are widely used in many industrial and research applications. Driven by advances in biology and nanotechnology, there is a growing need for performing such analyses at the microscale. A good example in point is the study of deformation and failure mechanisms of complex material systems. Detailed experimental full-field characteristics, in combination with theoretical and/or computational modeling, can provide crucial information in helping establish their microstructure-property relationships.

There are a range of optical techniques for measuring height profiles and displacements in 3D. Existing optical surface-profiling techniques can be divided into two categories: spatial-scanning methods and full-field methods. The first category includes scanning-laser confocal microscopy [21-23], chromatic depth scanning method [24], and laser spot scanning or line scanning approaches. All of these methods are intrinsically point-wise or line-wise scanning methods, but can achieve full-field measurement by means of spatial scanning. In the second category of inherent full-field methods, topographic reconstruction is done by processing two-dimensional optical images. Some of the commonly used full-field methods include white light and laser interferometry [47], projection Moire interferometry [29], depth from focus/defocus (DFF/DFD) [30-32], as well as three-dimensional (3D) digital image correlation (DIC) [33, 34, 48]. In general, the full-field methods allow much faster 3D topographic imaging than the spatial-scanning methods.

A small number of approaches are available for 3D full-field surface displacement measurement. Among them, electronic speckle pattern interferometry (ESPI) [49] offers

the highest sensitivity but suffers from very limited measurement range due to speckle decorrelation. In recent years, 3D-DIC is being increasingly used for 3D deformation characterization for its ease of operation.

Despite the advent of the above measurement techniques, high-accuracy 3D surface deformation and profile characterizations at the microscale, however, remain a great challenge. Traditional optical microscopes can achieve sub-micron spatial resolution, but they are only capable of two-dimensional (2D) imaging. In a recent study, Li and Yi developed a freeform prism array that could be attached to the objective of a microscope to enable 3D stereo imaging [50]. They demonstrated the viability of their method through quantitative 3D imaging tests, but did not provide an imaging processing algorithm for quantitative 3D shape reconstruction.

Xia et al. has recently developed a novel image correlation-based technique, named DAIC, for 3D full-field deformation and profile measurement [51]. The DAIC method utilizes a transmission grating and a single camera to achieve 3D perception, making it particularly suitable for both macroscopic and microscopic measurements. In this paper, we present a novel 3D microscope that has been newly developed by seamlessly integrating the DAIC technique with an optical microscope. The microscope has a unique capability of 3D deformation and morphology measurement with sub-micron spatial resolution. In the remainder of this paper, we will first describe the experimental setup of the microscope, followed by a description of the data analysis method. We will then present and discuss the results of a series of validation tests. Finally, concluding remarks will be given in the end.

3.2 Theory

3.2.1 Decoding of 3D Surface Displacement

The 3D displacements of the specimen (*P*) and its intermediate image (*P'*) are assumed to be related according to the following linear relationship:

$$u_{p'} = M_{xy} u_p + \alpha_x (x - x_c) w_p \tag{3.1a}$$

$$v_{p'} = M_{xy} v_p + \alpha_y (y - y_c) w_p \tag{3.1b}$$

$$w_{p'} = M_z w_p \tag{3.1c}$$

in which M_{xy} and M_z are the in-plane and out-of-plane magnification factors, α_x and α_y are the coupling coefficients that account for the non-telecentricity of the imaging system, and x_c and y_c are the coordinates of the center of perspective projection. The 3D displacement of the intermediate image is further related to the in-plane displacements of the two first-order diffracted images (P''_- and P''_+) through [15]

$$u_{p''_-} = N_{xy} (u_{p'} + w_{p'} \tan\theta) \tag{3.2a}$$

$$u_{p''_+} = N_{xy} (u_{p'} - w_{p'} \tan\theta) \tag{3.2b}$$

$$v_{p''_-} = v_{p''_+} = N_{xy} v_{p'} \tag{3.2c}$$

where N_{xy} is the magnification factor of objective 3 and θ is the first-order diffraction angle of the grating.

By substituting Eqs. (3.2a)-(3.2c) into Eqs. (3.1a)-(3.1c) and inverting the resulting equations, we obtain the 3D displacement of the specimen as:

$$w_p = \frac{1}{2 N_{xy} M_z \tan\theta} (u_{p''_-} - u_{p''_+}) = \beta_1 \frac{(u_{p''_-} - u_{p''_+})}{2} \tag{3.3a}$$

$$u_p = \frac{1}{2N_{xy}M_z}(u_{p''_-} + u_{p''_+}) - \frac{\alpha_x(x-x_c)}{M_{xy}} w_p = \beta_2 \frac{(u_{p''_-} + u_{p''_+})}{2} - \beta_3(x-x_c)w_p \qquad (3.3b)$$

$$v_p = \frac{1}{2N_{xy}M_z}(v_{p''_-} + v_{p''_+}) - \frac{\alpha_y(y-y_c)}{M_{xy}} w_p = \beta_2 \frac{(v_{p''_-} + v_{p''_+})}{2} - \beta_4(y-y_c)w_p \qquad (3.3c)$$

Once the in-plane displacement fields of the two first-order diffracted views are obtained, the above equation can be used to calculate the 3D full-field displacement of the specimen. The free parameters of the optical system, β_i ($i = 1-5$), can be calibrated against a known 3D displacement field.

3.2.2 Decoding of 3D Surface Profile

3D profile measurement of a curved surface involves determining the surface height, h, as a function of in-plane coordinates, x_p and y_p. To derive a governing equation for profile measurement, we consider a virtual process in which the surface is initially flat and is deformed into the final curved shape with an out-of-plane displacement of $w = h$. Let $X_{p''_-}$ and $X_{p''_+}$ denote the initial *x*-coordinates of the first-order diffracted images and $x_{p''_-}$ and $x_{p''_+}$ denote the corresponding *x*-coordinates in the final configuration. According to Eq. (3.3a), we have

$$w(x_{p''_-}, y_{p''_-}) = \frac{\beta_1}{2}(u_{p''_-} - u_{p''_+}) = \frac{\beta_1}{2}[(x_{p''_-} - X_{p''_-}) - (x_{p''_+} - X_{p''_+})] = -\frac{\beta_1}{2}u_{p''} + C \qquad (3.4)$$

in which $u_{p''} = x_{p''_+} - x_{p''_-}$ is the relative displacement between the two first-order diffracted views in the final configuration, and $C = \frac{\beta_1}{2}(X_{p''_+} - X_{p''_-})$ is the relative displacement in the initial configuration. Here C is a constant, since the surface is made to be flat in the initial configuration.

Then we map w from the coordinate space of the diffracted views to that of the specimen to obtain:

$$h(x_p, y_p) = w(\frac{x_p}{\beta_2}, \frac{y_p}{\beta_2}) = -\beta_1 u_{p''} \tag{3.5}$$

In writing the above equation, we have dropped the constant term, C. This causes a shift in the measured profile but does not affect the actual shape of the specimen. The full-field distribution of $u_{p''}$ can be measured by correlating the two first-order diffracted images with the DIC method, and Eq. (3.5) can then be used to obtain the surface profile of the specimen.

3.3 Experiment

Figure 8 shows the schematic and actual experimental setup of the newly developed 3D microscope system. A Cartesian coordinate system $o(x, y, z)$ used throughout the study is also shown in the figure. The layout of the microscope closely resembles that of an epi-illuminated fluorescence microscope. Two infinity-corrected microscope objectives (objectives 1 and 2) (Nikon CFI Plan Apo 20x, N.A. 0.75 and Olympus UPlanFL N 20x, N.A. 0.50) are placed back to back and are used to form an intermediate

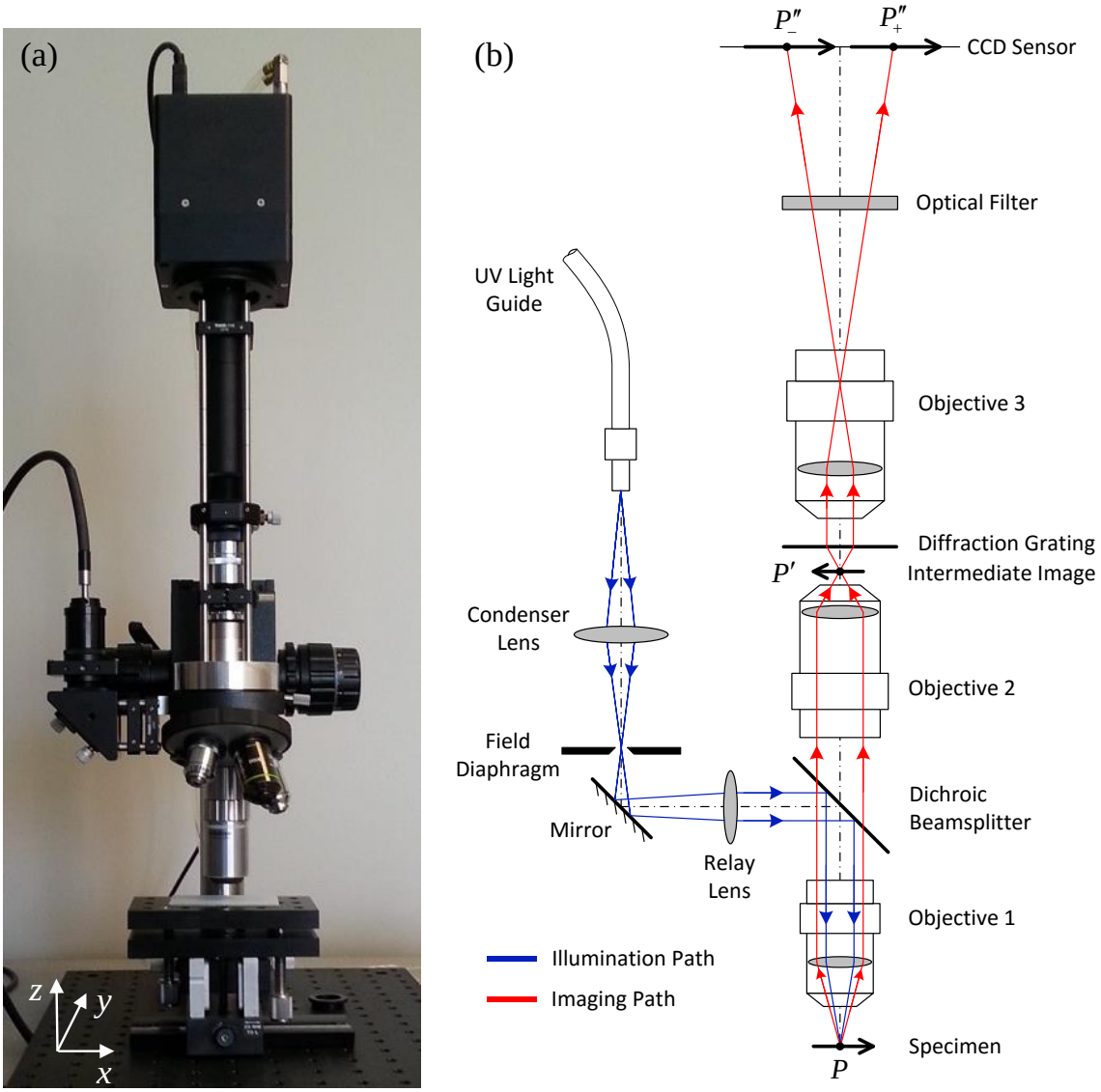

Figure 8. (a) Photograph of the newly developed optical microscope for three-dimensional (3D) surface displacement and profile measurements; (b) schematic layout of the microscope.

real image (*P'*) of a micro-sized specimen (*P*). A custom-made transmission diffraction grating (Ibsen Photonics, Denmark) is positioned right above the real image. The grating has a constant line spacing of 2000 nm, and a rectangular profile specially designed to suppress the zeroth-order light diffraction and enhance the intensity of the two first-order

diffracted beams. The ruling of the grating is aligned with the *y*-direction. Therefore, diffraction by the transmission grating along the *x*-direction creates two first-order virtual images of the intermediate real image. A third microscope objective (objective 3, Nikon BD Plan 20x , N.A. 0.4) is used to project the virtual images onto the senor plane of a high-resolution, Peltier-cooled CCD camera with 16-bit digital digitization (ML8300M, Finger Lakes Instrumentation, Lima, New York).

Illumination of the specimen is provided by an ultraviolet (UV) light-emitting diode (LED) light source (GCS-0365-07, Mightex Systems, Toronto, Canada). An iris field diaphragm is positioned in the illumination path so that the size and location of the illuminated area can be precisely controlled. A narrow-band-pass filter (450±10 nm bandpass, Thorlabs Inc, Newton, NJ) is inserted in the imaging path, to filter out the background light as well as to suppress chromatic dispersion of the transmission grating. The entire setup is placed on a vibration isolation table to reduce external vibrations.

The 3D surface displacement or profile of the specimen is encoded in the projected first-order images (P''_{-} and P''_{+}). Decoding of such 3D data requires two-dimensional (2D) full-field displacement analysis of the first-order diffracted images. In the present work, this analysis is carried out using the 2D digital image correlation (DIC) method [16-18]. A random speckle pattern required for the implementation of DIC is created by coating the specimen surface with fluorescent polymer particles of diameters between 1-5 microns (FMB-1UM-5UM, Cospheric LLC, Santa Barbara, CA).

3.4 Results

3.4.1 3D Surface Displacement Measurement

Rigid-body translation and rotation experiments were conducted to assess the validity of the 3D microscope system for displacement measurement. A flat glass slide speckled with fluorescent particles was used as a test specimen in the both experiment. Fig. 9 shows the negative first (-1) and positive first (+1) diffraction order views of a selected region on the glass slide, each of which has a field of view of 320 μm × 340 μm and a pixel resolution of 0.53 μm/pixel. Note that the zeroth-order view, which corresponds to direct light transmission through the grating, does not show up due to strong intensity suppression of the zeroth-order diffraction.

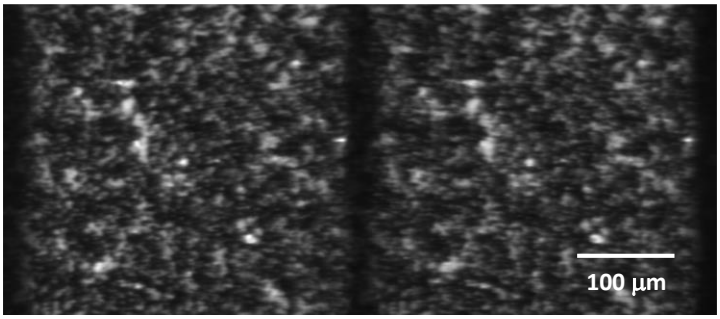

Figure 9. The negative and positive first-order views of a speckle-patterned region on a flat glass slide.

In the rigid-body translation experiment, the glass slide was translated along the vertical (z) axis for 10.0 μm using a differential micrometer driven translation stage (PT1A, Thorlabs Inc, Newton, NJ). Four speckle images, including two negative first-order (-1st) images and two positive first-order (+1st) images were captured before and after the rigid-body translation. 2D-DIC analysis was carried out between the -1st order

images and between the +1st order images, yielding two sets of in-plane displacements ($u_{p_-''}$, $v_{p_-''}$) and ($u_{p_+''}$, $v_{p_+''}$) as shown in Fig. 10. Because light diffraction only acts in the *x* direction, the two *y*-displacement maps are nearly identical. In contrast, the two *x*-displacement maps encode the out-of-plane displacement of the specimen in different ways, and therefore exhibit a large difference (note the difference in the displacement ranges). The specimen does not have any in-plane motion. However, all of the four displacement fields are linearly varying with similar gradient magnitudes, indicating that the non-telecentricity of the microscope is significant.

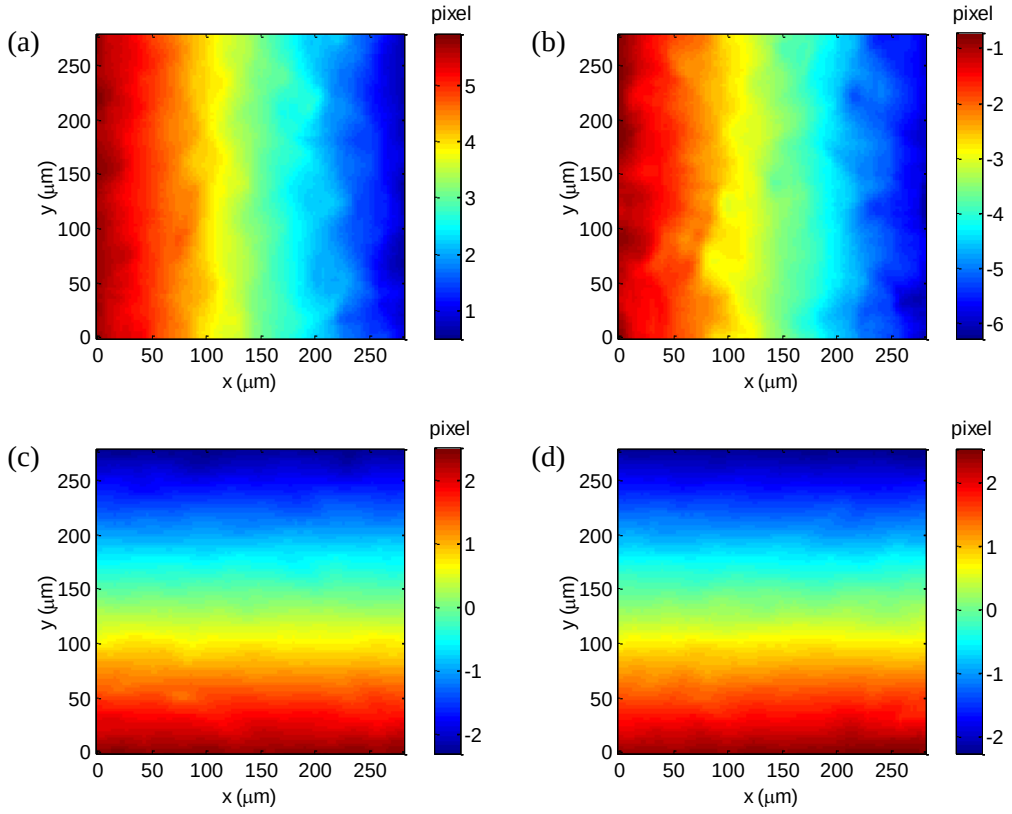

Figure 10. In-plane displacement maps of the two first-order diffracted views due to an out-of-plane rigid-body translation of 10.0 μm: (a) negative first order ($u_{p_-''}$); (b) positive first order ($u_{p_+''}$); (c) negative first order ($v_{p_-''}$); (d) positive first order ($v_{p_+''}$).

The four displacement maps shown in Fig. 10 were used in Eq. 3.3(a)-(c) to calculate the in-plane displacements (u_p, v_p) and out-of-plane displacement (w_p) of the specimen. The optical parameters in these equations were obtained by least-squares fitting the calculated displacements to the actual imposed displacements. Fig. 11(a)-(c) shows the contour plots of the calculated in-plane and out-of-plane displacement components. The displacement profiles along the central horizontal line are plotted in Fig. 11(d).

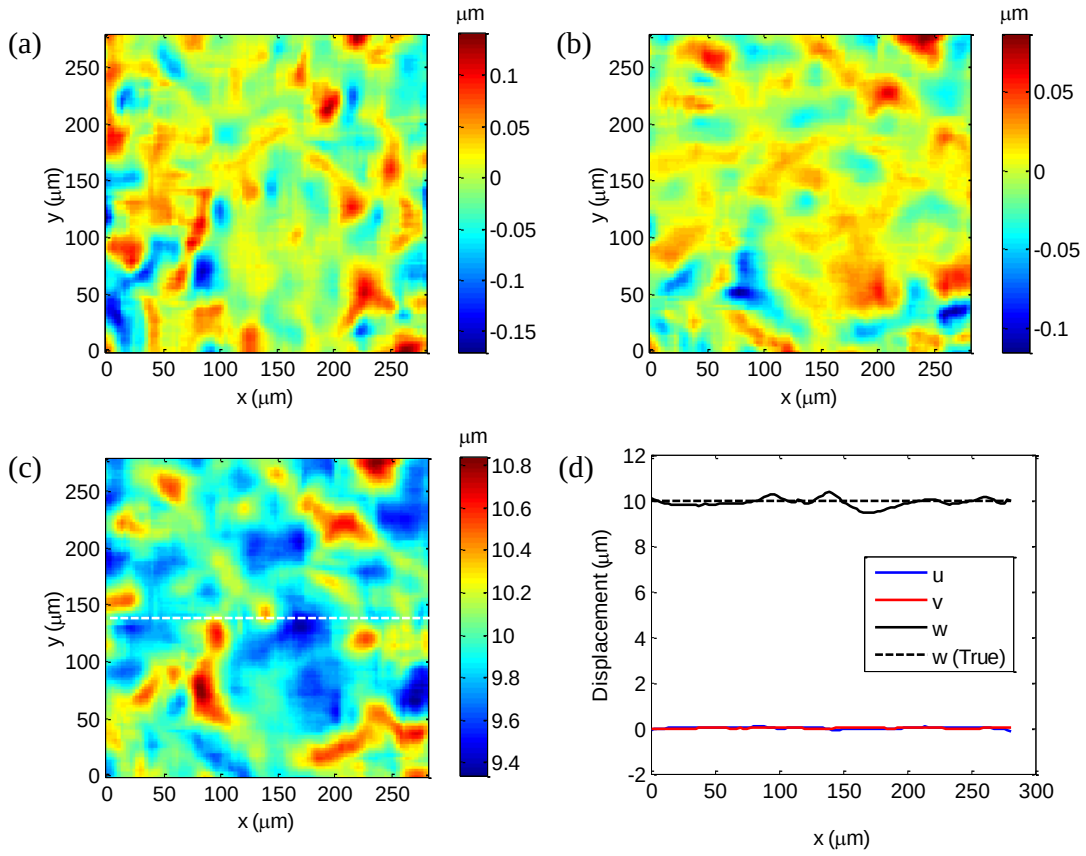

Figure 11. Measured 3D displacement fields due to an out-of-plane translation of 10.0 μm: (a) u_p; (b) v_p; (c) w_p; (c) displacement profiles along the dashed section line shown in (c).

To further demonstrate the measurement capability of the microscope, a second experiment was carried out in which the glass side was tilted about an axis along the *y*-direction for 6.0 degrees using a tilt stage. The tilt produced constant in-plane displacement components and a linearly varying out-of-plane displacement field. Similar to the first experiment, four in-plane displacement components of the first-order diffracted views were measured. The previously calibrated optical parameters were used to calculate the 3D displacements from these in-plane displacement maps. The obtained 3D displacement fields are presented in Fig. 12(a)-(c). Fig. 12(d) shows the measured 3D displacement profiles along the dashed section line in Fig. 12(c), together with the true out-of-plane displacement profile. The measured and true out-of-plane displacements compare favorably with each other.

3.4.2 3D Surface Profile Measurement

The surface profiling capability of the microscope was tested by profiling the top surface of a steel ball (0.68 mm in diameter). The two first-order diffracted views of the test surface are shown in Fig. 13(a). The microscope was focused near the central region of the field of view. Hence, the perimeter of the field of view was noticeably out of focus. The central in-focused regions in the two diffracted views were correlated using the DIC method. The resulted *x*-displacement field was substituted in Eq. (3.5) to obtain the topography of the test surface as shown in Fig. 13(b). Comparison between the measured and true height profiles along two section lines is given in Fig. 13(c). A good level of agreement is found, especially near the central region of the field of view.

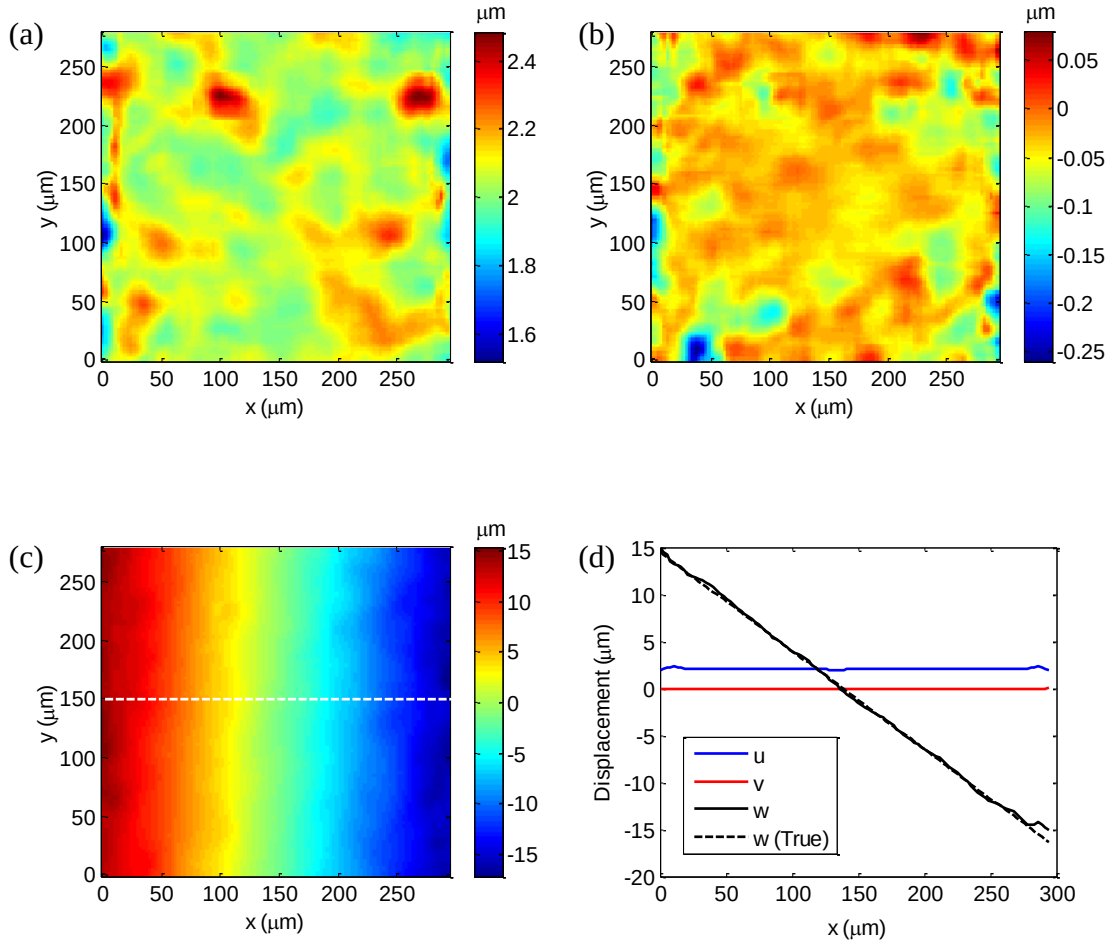

Figure 12. Measured 3D displacement fields due to an out-of-plane tilt: (a) u_p; (b) v_p; (c) w_p; (c) displacement profiles along the dashed section line shown in (c).

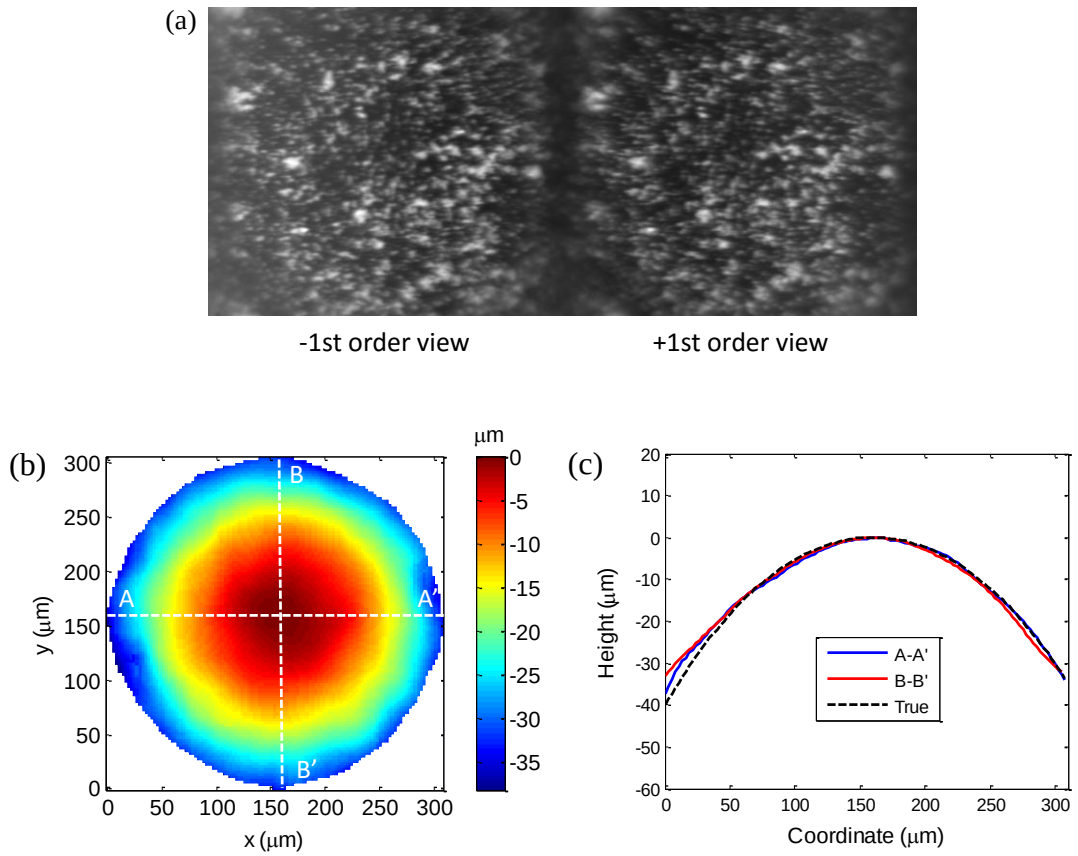

Figure 13. (a) The negative and positive first-order views of a speckle-patterned spherical surface; (b) measured topography of the test surface; (c) height profiles along the two dashed section lines shown in (b).

3.4.3 Error Assessment

The root-mean-square (RMS) errors for all the measured data are tabulated in Table 1. The two sets of profile data show comparable errors at the sub-pixel level. The largest error occurs in the out-of-plane (z) direction and the least in the y-direction along which no diffraction occurs. The measured profile shows a large error of 1.345 μm (2.54 pixels), mainly due to image blurring in the perimeter of the measured area.

Table 1. Root-mean-square (RMS) errors in 3D displacement and profile measurements.

Component	3D Displacement Measurement		3D Profile Measurement (μm)
	Rigid-body translation (μm)	Rigid-body rotation (μm)	
u_p	0.038	0.084	–
v_p	0.022	0.031	–
$w_p(h)$	0.232	0.296	1.345

3.5 Conclusions

In conclusion, we have presented an optical microscope system for full-field, noncontact measurements of 3D surface deformation and topography at the microscale. The 3D microscope system was developed by a novel combination of the DAIC method and fluorescent microscopy. The theoretical basis for data analysis and processing was provided. The performance of the system was tested by measuring the 3D displacement components of rigid-body translation and rotation, as well as by profiling the top surface of a micro-sized ball. With the submicrometer spatial resolution and subpixel measurement accuracy demonstrated here, the 3D microscope can serve as a unique tool in biological and materials research, as well as in quality engineering and inspection.

CHAPTER 4

DIFFRACTION ASSISTED LIGHT FIELD MICROSCOPY

4.1 Introduction

3D microtomography is playing increasingly prominent roles in medical imaging [52-54], biological and material characterization [55-57]. The existing 3D measurement techniques can be mainly categorized as the stylus based microscopy and noncontact microscopy. The first group includes scanning probe microscope and stylus profilometry. They are inherently pointwise methods that are based on a scanning tip to obtain the profile of a target surface. In the latter group, there are a wide range of techniques, such as 3D electron beam tomography [58], optical microscopy and magnetic resonance imaging [59]. 3D electron microscopy involves the combination of a conventional electron microscope, such as scanning electron microscope, transmission electron microscope and reflection electron microscope, with a 3D image reconstruction method. Superior to the above mentioned 3D electron microscope, optical methods offer unique advantages, such as non-intrusive measurement capability, fast sampling speed and no potential harm to the live cells or tissues [60, 61].

Current 3D optical microscopy includes deconvolution, confocal microscopy and optical coherence tomography [6]. All of these methods generate 3D data with a point by point or layer by layer scanning method, i.e. optically sectioning the specimen, which physically imposes constraints on the maximum thickness on the specimen that could be imaged. Another worth mentioning 3D imaging method, diffraction assisted image correlation microscope developed by Xia and coworkers [60], is intrinsically a full field

method that can get the 3D surface profile of a specimen in a single shot with high accuracy. But the reduced depth of focus greatly limits the maximum depth of the specimen that can be measured at high magnification. Extensive efforts, by using specially designed optical path, structured light illumination or improved deconvolution algorithms, have been devoted to overcoming the shallow depth of focus limitation [62-64].

The recently developed light field microscopy can reconstruct the volumetric data of a specimen with extended depth of field in a single shot [12, 13]. But the performance of the system is greatly constrained by the poor axial resolution. In the current study, we will show that by inserting a diffraction grating between the imaging specimen and the objective lens, two first-order diffracted light field images could be formed in the camera sensor plane and used for tomographic reconstruction. We show that the axial resolution of the reconstructed 3D volumetric data can be greatly improved by a diffraction assisted light field rendering method without sacrificing the lateral resolution.

4.2 Theory

The volume reconstruction from the diffraction assisted light field microscopy (DLFM) involves deconvolution of a diffracted light field image with a point spread function of the imaging system. To be more specific, we need to invert a linear forward imaging model,

$$\mathbf{f} = \mathbf{G}\mathbf{g}, \tag{4.1}$$

where $\mathbf{f}$ is the diffracted light field image, $\mathbf{g}$ is the 3D volume to be reconstructed and $\mathbf{G}$ is the forward transformation matrix of the imaging system.

4.2.1 Light field point spread function

The point spread function (PSF) of an imaging system is critical to characterizing its imaging capability. In a DLFM, the point spread function is spatially invariant, which is different from the Airy pattern of a simple microscope. To analytically model the point spread function of the DLFM, monochromatic light illumination with a wavelength of λ is assumed here. This is a reasonable assumption when a narrow-band optical filter is inserted in the optical path of the microscope. In a typical light field microscope, the two key optical components are the objective lens and microlens array. The wave distribution $\mathbf{X} = (x, y)$ on the native image plane of the objective from a point source located in the 3D volume at $\mathbf{V} = (V_1, V_2, V_3)$ can be easily obtained based on the above assumption, which reads

$$U(\mathbf{X}, \mathbf{V}) = \frac{M}{\lambda^2 f^2} \exp\left(-\frac{iu}{4\sin^2\frac{\alpha}{2}}\right) \int_0^{\alpha} P(\theta) \exp\left(-\frac{iu\sin^2\frac{\theta}{2}}{2\sin^2\frac{\alpha}{2}}\right) J_0\left(\frac{\sin\theta}{\sin\alpha} v\right) \sin\theta d\theta , \tag{4.2}$$

where M and f are the magnification factor and focus length of the objective, respectively. The wave number $\kappa = \frac{2\pi n}{\lambda}$ and angle of the numerical aperture $\alpha = \sin^{-1}\frac{NA}{n}$ are calculated from the wavelength λ and refractive index n. J_0 is the zeroth-order Bessel function, u and v are the normalized optical coordinates,

$$u = 4\kappa V_3 \sin^2\frac{\alpha}{2}, \tag{4.3}$$

$$v = \kappa\sqrt{(x - V_1)^2 + (y - V_2)^2}\sin\alpha . \tag{4.4}$$

The function $P(\theta)$ can be simplified as $p(\theta) = \cos^{1/2}\theta$ in an Abbe-sine corrected lens.

After the PSF calculation for the objective lens, we will need to consider the light transmission through the microlens array. For a microlens array with focus length d and pitch p, its PSF can be modeled as

$$\phi(\mathbf{X}) = rec(\mathbf{X}/p)\exp(\frac{-i\kappa}{2d}\|\mathbf{X}\|_2^2)comb(\mathbf{X}/p)\,. \tag{4.5}$$

With a Fresnel propagation approach to model the light transport from the microlens array to the camera sensor plane, the overall PSF can be described as

$$h(\mathbf{X},\mathbf{V}) = F^{-1}\left\{F[\phi(\mathbf{X})U(\mathbf{X},\mathbf{V})]\exp[-\frac{i}{4\pi}\lambda d(w_x{}^2 + w_y{}^2)]\right\} \tag{4.6}$$

where w_x and w_y are the spatial frequencies of the light along the *x*- and *y*-directions of the camera sensor plane.

To computationally determine the PSF, a discretization process is required. Let the camera sensor have $C_x \times C_y$ pixels and the volume $\mathbf{V}$ be divided into $V_1 \times V_2 \times V_3$ voxels. A transformation matrix h_{ij} indicating the projection of light from voxel i to pixel j can be integrated as

$$h_{ij} = \int_{A_j}\int_{V_i} w_i(\mathbf{V})|h(\mathbf{X},\mathbf{V})|^2 d\mathbf{V}d\mathbf{X}\,, \tag{4.7}$$

where A_j is the area of pixel j, V_i is the volume of voxel i, and $w_i(\mathbf{V})$ is the sampling filter that weights the contribution at the center of the voxel more than its edge. A raised cosine window with width three times of the volume sampling period is used in the current study.

4.2.2 Image reconstruction

With the insertion of a diffraction grating, diffracted views of the specimen with different orders appear symmetrically about the zeroth-order view. In the current work, only the first-order positive and negative images are considered, which can be taken as the projections from two virtual objects $\mathbf{V}^{+}$ and $\mathbf{V}^{-}$. By an optical ray-tracing method [36, 51], the coordinates of the two virtual objects can be described as

$$\mathbf{V}^{\pm 1} = \begin{bmatrix} \mathbf{D}_{+} \\ \mathbf{D}_{-} \end{bmatrix} \cdot \mathbf{g} = (V_1 \mp V_3 \tan\theta, V_2, {V_3}/{\cos^3\theta}) \tag{4.8}$$

where $\mathbf{D} = [\mathbf{D}_{+} \quad \mathbf{D}_{-}]^T$ is transformation matrix of the diffraction grating, and $\theta = \sin^{-1}({\lambda}/{p})$ is the diffraction angle determined by wavelength λ and grating pitch p. Combining Eqs. (4.1) and (4.8), the diffraction assisted imaging model can be represented as

$$\begin{bmatrix} \mathbf{f}_{+} \\ \mathbf{f}_{-} \end{bmatrix} = \begin{bmatrix} \mathbf{G}_{+} \\ \mathbf{G}_{-} \end{bmatrix} \mathbf{g}, \tag{4.9}$$

where $[\mathbf{G}_{+} \quad \mathbf{G}_{-}]^T = \mathbf{DH}$ is the total transformation matrix. In the current image deconvolution process, a Richardson-Lucy (RL) iteration [65] scheme is implemented as

$$\mathbf{g}^{(n+1)} = (\mathbf{G}_{+}^{-1}\mathbf{f}_{+} + \mathbf{G}_{-}^{-1}\mathbf{f}_{-})(\mathbf{G}_{+}^{-1}(\mathbf{G}_{+}\mathbf{g}^{(n)}) + \mathbf{G}_{-}^{-1}(\mathbf{G}_{-}\mathbf{g}^{(n)}))^{-1}\mathbf{g}^{(n)} \tag{4.10}$$

to reconstruct the volumetric data.

4.3 Experimental Results

In the current experiment, the original DAIC fluorescent microscope was modified by inserting a microlens array (Fresnel Technologies, Inc. Fort Worth, TX) between the objective 3 and the camera. A microlens array with pitch of $125\mu m$ and focus length $2500\mu m$ was selected to match the numerical apertures (NAs) of the objective 3 and the microlenses. In order to minimize the modification of the camera, a 1:1 relay lens (Thorlabs, Inc. Newton, NJ) was placed in front of the camera to extend the distance between the microlens array and the camera sensor plane. A schematic illustration of the proposed optical system for the DLFM is shown in Fig. 14 (a). A commercially available transmission grating (Ibsen Photonics, Denmark) with a pitch of 2000 nm was used here. The position of the diffraction grating was carefully adjusted to ensure that there were no overlaps between the two diffracted first-order views. The microlens array was placed in the image plane of objective 3. The camera sensor plane was located right in the back focus plane of the relay lens to ensure all the sub-images appropriately fill the camera sensor without overlap or big gaps between them. Fig. 14 (b) shows the positive first-order and negative first-order diffracted light field views of a point light source.

A single $12\mu m$ diameter light yellow fluorescent particle (Spherotech, Inc. Lake Forest, IL) was used for imaging. A monochromatic light with a wavelength of 450 nm was chosen for illumination. A diffraction assisted light field deconvolution was carried out with a RL scheme for 8 iterations to reconstruct the particle, as described in equation (4.8). In Figs. 15(a) and (b), we show the comparison of the reconstructed images both from a traditional light field microscope and our diffraction assisted light field microscope. The reconstructed image resolution from the DLFM is found to be worse

than that from a traditional light field method. This could be due to the small diffraction angle of the grating used in our experiment.

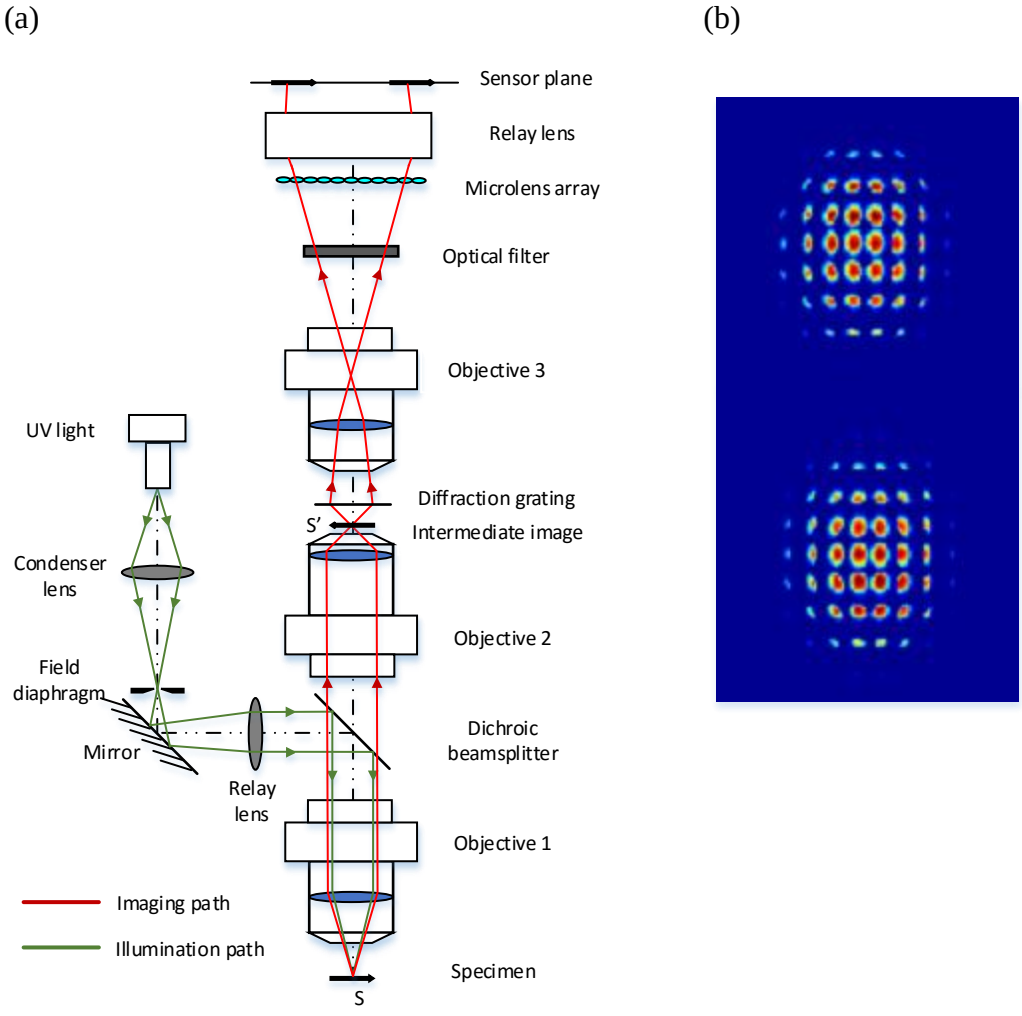

Figure 14. (a) Schematic layout of the diffraction assisted light field microscope for 3D tomography measurement; (b) the positive and negative first-order light field images of a point light source.

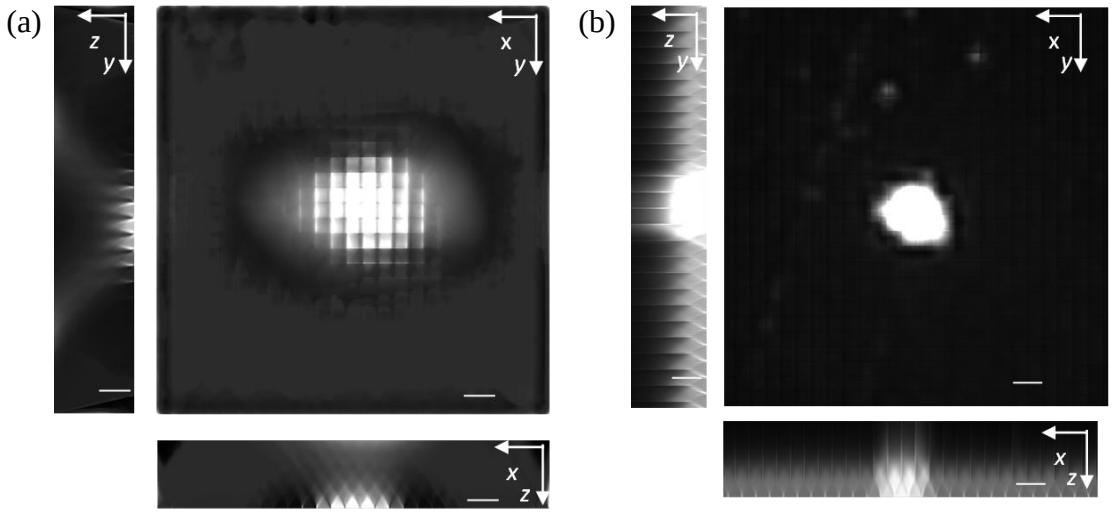

Figure 15. Maximum intensity projections (MIPs) of a fluorescent particle with diameter $12\mu m$ from the (a) DLFM and (b) traditional light field microscope. The scalar bars are $10\mu m$.

4 Simulation Results

To achieve a larger diffraction angle which cannot be easily implemented in the current experimental setup, a set of simulated experiments was conducted. A standard 20x objective lens with a numerical aperture (NA) 0.5 was used. To match the image-side NA of the objective, a microlens array with pitch $150\mu m$ and focus length $3000\mu m$ was

selected. A monochromatic light with a wavelength of 450 nm was chosen for illumination.

A diffraction grating with a pitch of 900 nm was selected here which could give a diffraction angle of $\theta = 30^o$ for light illumination with 450 nm wavelength. The PSF was constructed with a sampling ratio of 3. Seven randomly distributed spherical fluorescent particles of diameter $12\mu m$, confined to a rectangular box ($256\mu m \times 256um \times 40um$) with its upper surface ($z = 40\mu m$) fixed at the focus plane, were used for reconstruction. The diffracted light field images of the random particles are shown in Figs. 16(a) and (b). A diffraction assisted light field deconvolution was carried out with a RL scheme for 8 iterations to reconstruct the particles, as described in Eq. (4.8).

From the maximum intensity projections (MIPs), the lateral resolution of the DLFM does not have significant improvement compared with a traditional light field rendering method [66] under the same reconstruction process, as shown in Figs. 16 (d) and (e). However, the improvement of the axial resolution is very striking, both when the particles are close to the focus plane and far away from the focus plane, as shown in Fig. 16 (e). Therefore, with the insertion of a diffraction grating, the resolving power of the light field microscope in the axial direction is greatly enhanced.

In a conventional microscope, only the orthographic view of a specimen can be obtained. By inserting a microlens array into the imaging path, one can capture light fields from the specimen and use them to resolve the axial information of the specimen. The axial resolution of a light field microscope is in general much worse than its lateral resolution. The insertion of a diffraction grating in the imaging path of the light field

microscope results in multiple diffracted views that encode the out-of-plane geometric information of the specimen. Therefore, decoding of such 3D information from the diffracted views allows one to perform 3D tomographic reconstruction with improved axial resolution.

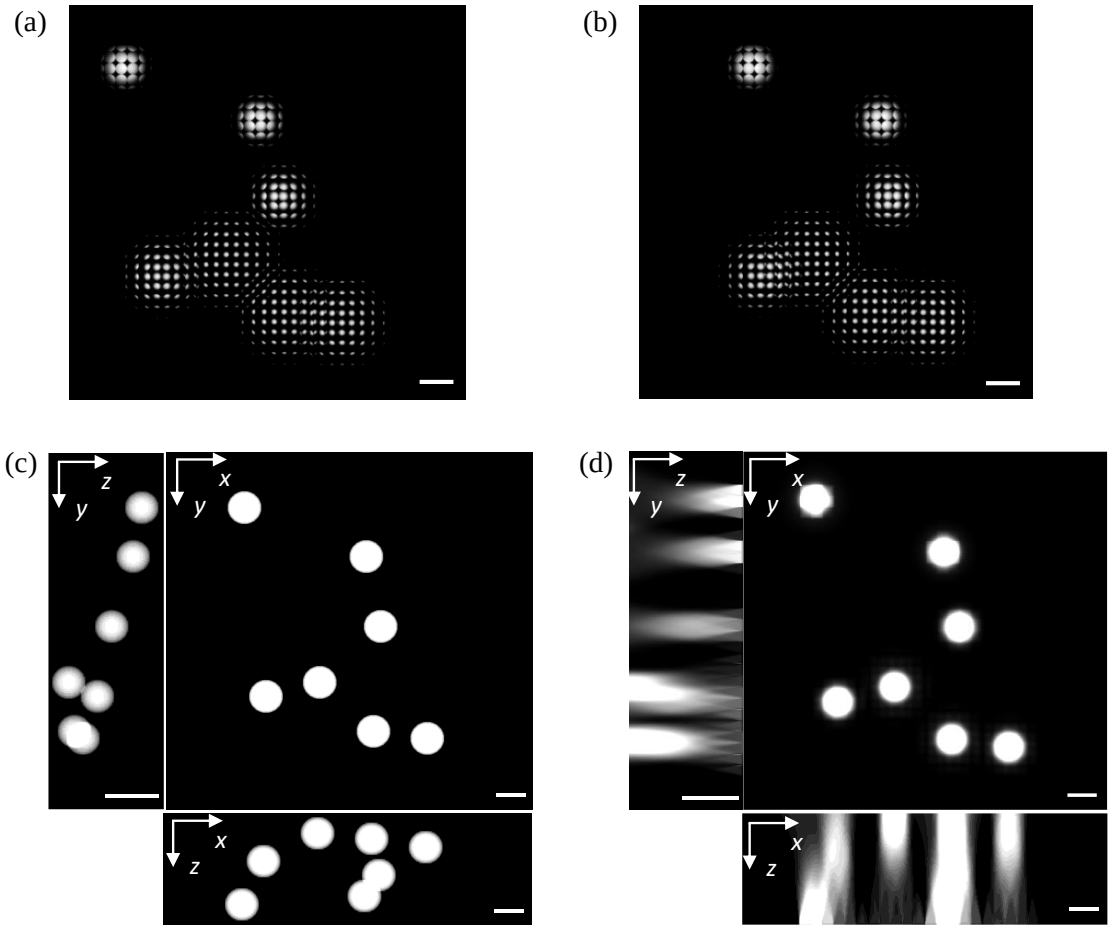

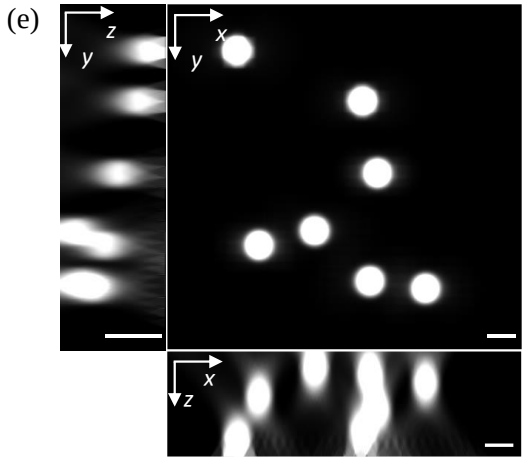

Figure 16. (a, b) Positive and negative first-order diffracted light field images of a set of randomly distributed fluorescent particles. (c) True MIPs of the fluorescent particles with diameter $12\mu m$. (d) MIPs reconstructed with the traditional light field rendering method. (e) MIPs reconstructed with the diffraction assisted light field rendering method. Both reconstruction processes are performed with 8 Richardson-Lucy (RL) iterations. The scale bars in all the images are $10\mu m$.

A set of diffraction gratings with different diffraction angles of 15º, 30º, and 45º are used to investigate the effect of diffraction angle on the resolution of tomographic reconstruction. As shown in Fig. 17, when the diffraction angle becomes lager, the lateral resolution remains largely unchanged. However, the axial resolution has significant improvement when the grating angle increases from 15º to 45º. This suggests that a large diffraction angle helps to encode more depth information in the diffracted views and therefore greatly improves the axial resolution of the measurement.

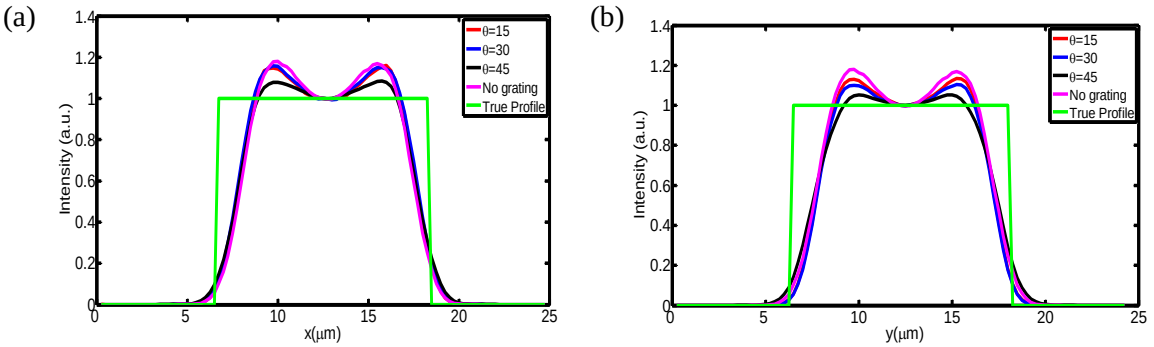

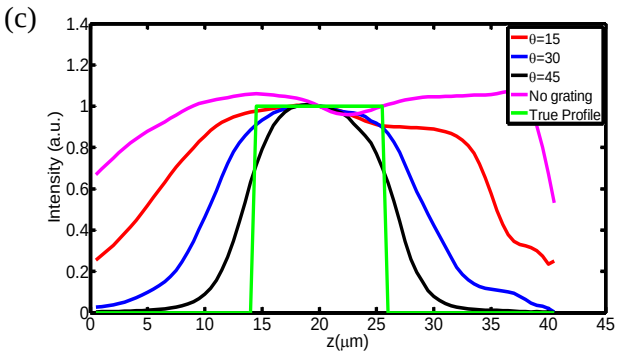

Figure 17. Comparison of the lateral and axial resolutions with different grating angles. (a, b) *x*- and *y*-direction profiles showing the lateral resolution. (c) *z*-direction profiles showing the axial resolution. (a.u.: arbitrary unit)

In a DLFM, the reconstruction of a 3D volume is based on the deconvolution of the PSF and the two first-order diffracted light field images. A parallel projection of the specimen is collected on the camera sensor plane as the diffracted light field images. The light ray density is varying with its distance from the focus plane. Accordingly, the axial resolution of the reconstructed 3D volume is dependent upon the spatial location of the sample. To examine this dependence, three fluorescent particles with diameter $12\mu m$ located at $7.5\mu m$, $20\mu m$ and $30\mu m$ away from the focus plane, respectively, are used for tomographic reconstruction. With the same reconstruction procedure, the obtained *z*-direction intensity profiles are shown in Fig. 18. The particle located at $20\mu m$ away from the focus plane has the best axial resolution among the three. In the proposed DLFM

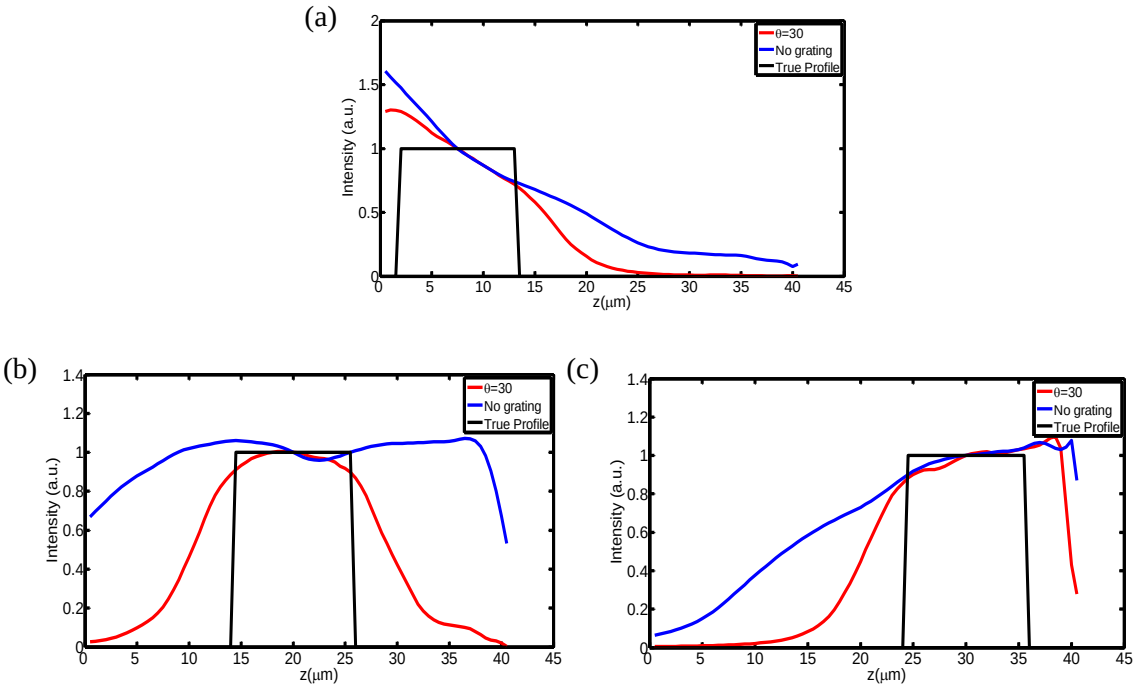

Figure 18. Comparison of the axial resolutions of a particle at varying distances from the focus plane, (a) $z = 7.5\mu m$,(b) $z = 20\mu m$,(c) $z = 30\mu m$. (a.u.: arbitrary unit)

reconstruction method, the light rays passing onto each pixel are projected back into the sample volume. The wider spread light rays could result in denser sampling pattern, which will permit finer reconstructed resolution. At the place near the focus plane where there is no such light ray spreading, the resolution enhancement is not obvious.

To investigate the bit depth effect on the reconstructed image resolution, two commonly used digital camera bit depth, 8 bit and 16 bit, are employed here. A particle located at $20\mu m$ away from the focus plane is used for reconstruction. Both the axial and lateral resolutions do not have obvious improvement by increasing the image bit depth

from 8 bit to 16 bit, as shown in Fig. 19. Therefore, in the current prototype, a commonly

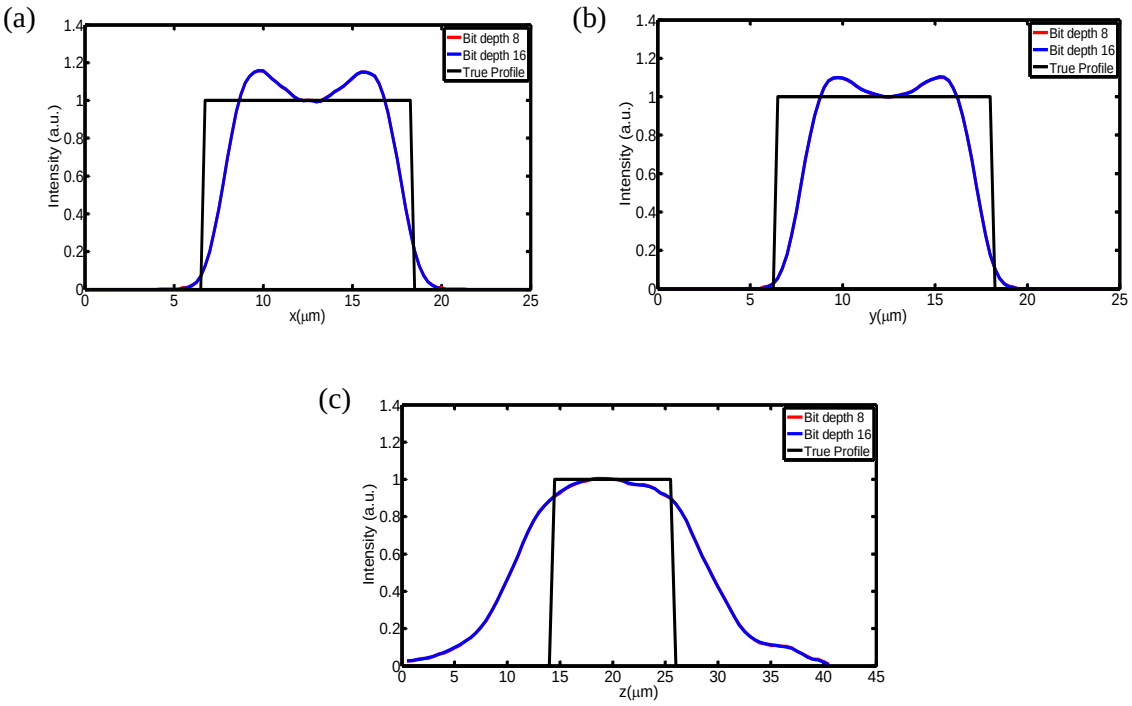

Figure 19. Effect of the bit depth on the lateral and axial resolutions. (a, b) *x*- and *y*-direction profiles showing the lateral resolution. (c) *z*-direction profile showing the axial resolution. (a.u.: arbitrary unit)

used 8 bit depth camera sensor could be more than enough to achieve the desired lateral and axial resolutions.

Equation (4.1) is a strict description of the noise free light field imaging process. To model a real imaging sensor system, it is necessary to include the noise effect. The standard RL deconvolution model can be viewed as a combination of the maximum likelihood algorithm with a Poisson statistical noise model [67]. For a typical CCD camera, the statistical Poisson noise assumption inherent in the RL algorithm results a very good convergence in the deconvolution process. A root-mean-square (RMS) value

$\mathrm{RMS} = \left|\mathbf{g}^n - \mathbf{g}\right| / \left|\mathbf{g}\right|$ is defined here to study the convergence rate of the RL algorithm for the diffraction assisted light field reconstruction, as shown in Fig. 20. The RMS error is seen to drop very fast at the first 8 iterations and finally converge to 0.675%.

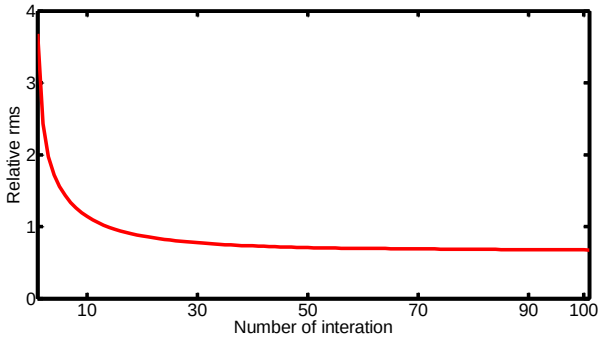

Figure. 20. $\left|\mathbf{g}^n - \mathbf{g}\right| / \left|\mathbf{g}\right|$ vs the number of iterations

Extensive research has been done on the blind deconvolution by the RL algorithm with Poisson statistic noise. However, the white noise is not thoroughly investigated in previous work which may also contribute to the divergence of the RL deconvolution [68]. In the current study, three different levels of white noise have been considered corresponding to a set of signal noise ratios (SNRs) of 1000, 100, 20, respectively. The obtained profiles indicate very good convergence even when the SNR is as low as 20, as shown in Fig. 21.

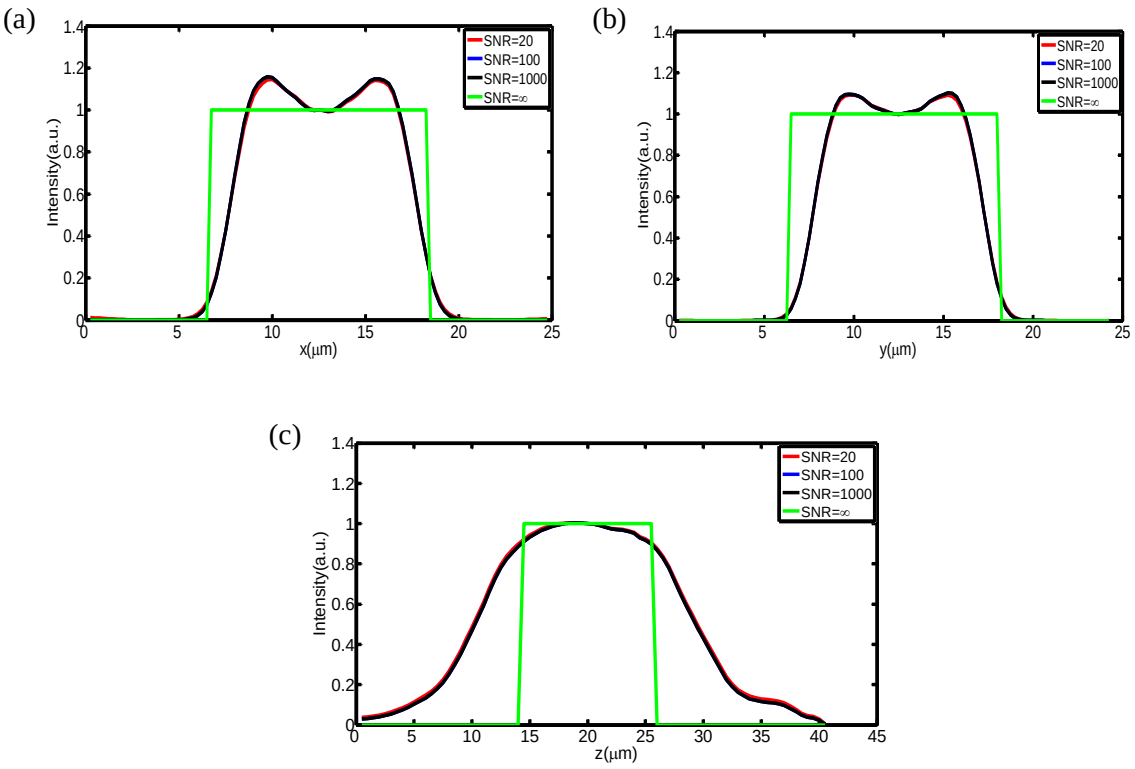

Figure 21. Effect of the white noise on the lateral and axial resolutions. (a, b) *x*- and *y*-direction profiles showing lateral resolution, (c) *z*-direction profile showing axial resolution. (a.u.: arbitrary unit)

4.5 Conclusions

In this chapter, a diffraction assisted light field reconstruction method is developed for 3D tomography measurement. This method involves the integration of a diffraction grating with a conventional light field microscope to achieve improved axial resolution. The theoretical outline of the diffraction assisted light field image reconstruction is proposed based on a wave optics model. The accuracy and capability of the microscope is validated via a set of simulated light field images. It is found that the axial resolution of

the reconstructed volumes has significant improvement compared to a conventional light field microscope without sacrificing the lateral resolution.

CHAPTER 5

CONCLUSIVE REMARKS

The research work in this thesis was stimulated by the development of a hybrid optical 3D deformation, displacement, and tomography measurement system that could be used for fast speed imaging with high accuracy. Our work shows that insertion of a transmission diffraction grating between a test specimen and camera lens results in diffracted views that encode 3D geometric information. The surface profile or deformation of the specimen can be obtained by performing 2D-DIC analysis of the two first-order diffracted views. Based on the DAIC method, a compact 3D microscope was developed for 3D deformation and displacement measurement at the microscale. The 3D microscope provides the following unique features that are not offered by any existing measurement techniques.

- Full-field, non-contact measurement of 3D displacement components and shapes of complex objects;
- A wide range of fields-of-view suitable for multiscale characterizations;
- High measurement accuracy (sub-pixel accuracy of ~10 nm at the smallest field-of-view).

We also showed that, by integrating the DAIC method with the light field microscopy, one could perform tomographic reconstruction at the microscale. The axial resolution of reconstructed 3D stacks was found to be greatly improved by the diffraction assisted light field rendering method without sacrificing the lateral resolution.

APPENDIX

ALIGNMENT PROCEDURE OF THE DAIC SETUP

Eqs. (2.7a)-(2.7c) are derived by assuming the optical axis of the camera is perpendicular to the transmission grating (i.e., the image plane is parallel to the grating surface) and the grating grooves are parallel to the *y*-axis of the image plane. In the current experiments, we carefully aligned the optical components in the setup to ensure satisfaction of this assumption. In our experiments, both the camera and the grating were mounted on 5-axis optical rail carriers to enable accurate alignment. The detailed alignment procedure is as follows:

1. Calibrate the intrinsic camera parameters (f_p, c_x, c_y) using a Camera Calibration Toolbox for Matlab [69]. f_c is the focal distance in pixels, and c_x and c_y are the principal point coordinates.
2. Align the optical axis of the camera parallel to an optical rail. This is done by placing an Iris aperture close in front of the camera. The aperture is translated in the *x*- and *y*-directions to align its center with the principal point of the camera on the display screen. The aperture is then translated to the far end of the optical rail, and the camera tilt about the *x*- and *y*-axes is adjusted to realign the aperture center with the principal point. This alignment process is performed iteratively until the aperture center is coincident with the principal point, regardless of the *z*-position of the aperture.

3. Mount a laser and point it at the camera lens, as shown in Fig. 8. The laser beam is made to be parallel to the optical rail (and the optical axis of the camera) using an iterative alignment process similar to that used in step 2.
4. Place two transmission gratings between the camera and the iris aperture, and pass the laser beam through one of the gratings. Bring the gratings to their operative position by adjusting their angular coordinates (θ_x and θ_y) and directing the reflected light beam through the iris aperture.
5. Bring the gratings close to the camera so that the 0^{th} order and 1^{st} order beams are collected by the camera. Adjust the gratings' angular position (θ_z) to align the three beam spots along the horizontal (x) direction on the display screen. In this way, the grating grooves are made to be parallel to the y-axis of the image plane.
6. Translate the grating holder along the x-direction, pass the laser beam through the other grating, and confirm proper alignment of this grating (The two gratings are mounted in a straight rectangular groove on the holder. Therefore, alignment of one grating would ensure alignment of the other).
7. Remove the gratings (together with the 5-axis carrier) from the optical rail.
8. Place a plane calibration board in front of the camera and set the camera to focus on the board. The calibration board contains a straight line of known physical length, L. The pixel length of this line is measured to be L' on the display screen. The pinhole-board distance, D, is determined according to $D = Lf_p/L'$.
9. Put the gratings back on the optical rail (together with the 5-axis carrier).

10. Measure the distance between the gratings and the calibration board, *d*, using a digital caliper. The distance between the camera pinhole (i.e., the optical center of the lens) and the grating, *s*, is calculated according to $s = D - d$.
11. Remove the calibration board. Place a test surface and perform profile measurement.

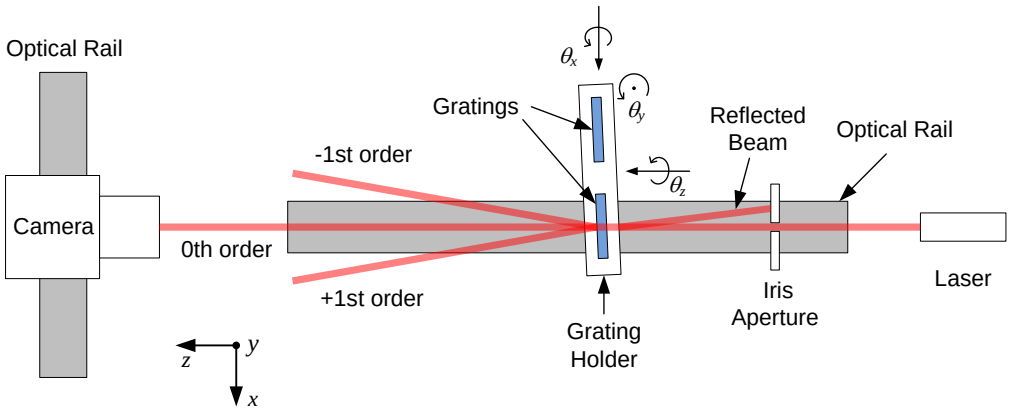

Figure 22. A schematic diagram of the experimental setup used for camera and grating alignment. A laser beam parallel to the z optical axis is used to assist in the alignment. The gratings shown in the figure are in a misaligned position, causing the reflected beam to deviate from being parallel to the z axis. The gratings are brought to their operative position by adjusting their angular coordinates (θ_x and θ_y) and directing the reflected light beam through the iris aperture.

REFERENCES

[1] Zhang, Z., 2012, "Review of single-shot 3D shape measurement by phase calculation-based fringe projection techniques," Optics and Lasers in Engineering, 50(8), pp. 1097-1106.

[2] Guastavino, R., and Göransson, P., 2007, "A 3D displacement measurement methodology for anisotropic porous cellular foam materials," Polymer testing, 26(6), pp. 711-719.

[3] Studholme, C., Hill, D. L., and Hawkes, D. J., 1999, "An overlap invariant entropy measure of 3D medical image alignment," Pattern recognition, 32(1), pp. 71-86.

[4] Surmann, H., Nüchter, A., and Hertzberg, J., 2003, "An autonomous mobile robot with a 3D laser range finder for 3D exploration and digitalization of indoor environments," Robotics and Autonomous Systems, 45(3), pp. 181-198.

[5] Sansoni, G., and Docchio, F., 2004, "Three-dimensional optical measurements and reverse engineering for automotive applications," Robotics and Computer-Integrated Manufacturing, 20(5), pp. 359-367.

[6] Chen, F., Brown, G. M., and Song, M., 2000, "Overview of three-dimensional shape measurement using optical methods," Optical Engineering, 39(1), pp. 10-22.

[7] Chu, T., Ranson, W., and Sutton, M., 1985, "Applications of digital-image-correlation techniques to experimental mechanics," Experimental Mechanics, 25(3), pp. 232-244.

[8] Pan, B., Qian, K., Xie, H., and Asundi, A., 2009, "Two-dimensional digital image correlation for in-plane displacement and strain measurement: a review," Measurement science and technology, 20(6), p. 062001.

[9] Berfield, T., Patel, J., Shimmin, R., Braun, P., Lambros, J., and Sottos, N., 2007, "Micro-and nanoscale deformation measurement of surface and internal planes via digital image correlation," Experimental Mechanics, 47(1), pp. 51-62.

[10] Pan, B., Xie, H., Yang, L., and Wang, Z., 2009, "Accurate measurement of satellite antenna surface using 3D digital image correlation technique," Strain, 45(2), pp. 194-200.

[11] Garcia, D., Orteu, J., and Penazzi, L., 2002, "A combined temporal tracking and stereo-correlation technique for accurate measurement of 3D displacements: application to sheet metal forming," Journal of Materials Processing Technology, 125, pp. 736-742.

[12] Broxton, M., Grosenick, L., Yang, S., Cohen, N., Andalman, A., Deisseroth, K., and Levoy, M., 2013, "Wave optics theory and 3-D deconvolution for the light field microscope," Optics express, 21(21), pp. 25418-25439.

[13] Levoy, M., Ng, R., Adams, A., Footer, M., and Horowitz, M., 2006, "Light field microscopy," ACM Transactions on Graphics (TOG), 25(3), pp. 924-934.

[14] Stampfl, J., Scherer, S., Gruber, M., and Kolednik, O., 1996, "Reconstruction of surface topographies by scanning electron microscopy for application in fracture research," Applied Physics A, 63(4), pp. 341-346.

[15] Caber, P. J., 1993, "Interferometric profiler for rough surfaces," Applied optics, 32(19), pp. 3438-3441.

[16] Park, Y., Best, C. A., Badizadegan, K., Dasari, R. R., Feld, M. S., Kuriabova, T., Henle, M. L., Levine, A. J., and Popescu, G., 2010, "Measurement of red blood cell mechanics during morphological changes," Proceedings of the National Academy of Sciences, 107(15), pp. 6731-6736.

[17] Bajaj, C. L., Bernardini, F., and Xu, G., "Automatic reconstruction of surfaces and scalar fields from 3D scans," Proc. Proceedings of the 22nd annual conference on Computer graphics and interactive techniques, ACM, pp. 109-118.

[18] Scott, W., Roth, G., and Rivest, J.-F., 2003, "View planning for automated 3D object reconstruction inspection," ACM Computing Surveys, 35(1).

[19] Son, S., Park, H., and Lee, K. H., 2002, "Automated laser scanning system for reverse engineering and inspection," International Journal of Machine Tools and Manufacture, 42(8), pp. 889-897.

[20] Beheim, G., and Fritsch, K., 1986, "Range finding using frequency-modulated laser diode," Applied optics, 25(9), pp. 1439-1442.

[21] Hamilton, D., and Wilson, T., 1982, "Three-dimensional surface measurement using the confocal scanning microscope," Applied Physics B, 27(4), pp. 211-213.

[22] Pawley, J., 2010, Handbook of biological confocal microscopy, Springer Science & Business Media.

[23] Paddock, S. W., 1999, "Confocal laser scanning microscopy," Biotechniques, 27, pp. 992-1007.

[24] Molesini, G., Pedrini, G., Poggi, P., and Quercioli, F., 1984, "Focus-wavelength encoded optical profilometer," Optics communications, 49(4), pp. 229-233.

[25] Blais, F., 2004, "Review of 20 years of range sensor development," Journal of Electronic Imaging, 13(1).

[26] Denisyuk, Y. N., "Photographic reconstruction of the optical properties of an object in its own scattered radiation field," Proc. Soviet Physics Doklady, p. 543.

[27] Chang, B. J., Alferness, R., and Leith, E. N., 1975, "Space-invariant achromatic grating interferometers: theory," Applied optics, 14(7), pp. 1592-1600.

[28] Sasaki, O., and Okazaki, H., 1986, "Sinusoidal phase modulating interferometry for surface profile measurement," Applied optics, 25(18), pp. 3137-3140.

[29] Welford, W., 1969, "Some applications of projected interference fringes," Opt. Acta, 16(3), pp. 371-376.

[30] Darrell, T., and Wohn, K., "Pyramid based depth from focus," Proc. Computer Vision and Pattern Recognition, 1988. Proceedings CVPR'88., Computer Society Conference on, IEEE, pp. 504-509.

[31] Grossmann, P., 1987, "Depth from focus," Pattern Recognition Letters, 5(1), pp. 63-69.

[32] Pentland, A. P., 1987, "A new sense for depth of field," Pattern Analysis and Machine Intelligence, IEEE Transactions on(4), pp. 523-531.

[33] Helm, J. D., McNeill, S. R., and Sutton, M. A., 1996, "Improved three‐dimensional image correlation for surface displacement measurement," Optical Engineering, 35(7), pp. 1911-1920.

[34] Luo, P., Chao, Y., Sutton, M., and Peters Iii, W., 1993, "Accurate measurement of three-dimensional deformations in deformable and rigid bodies using computer vision," Experimental Mechanics, 33(2), pp. 123-132.

[35] Sutton, M. A., Orteu, J.-J., and Schreier, H. W., 2009, Image correlation for shape, motion and deformation measurements: basic concepts, theory and applications, Springer.

[36] Xia, S., Gdoutou, A., and Ravichandran, G., 2013, "Diffraction Assisted Image Correlation: A Novel Method for Measuring Three-Dimensional Deformation using Two-Dimensional Digital Image Correlation," Experimental Mechanics, 53(5), pp. 755-765.

[37] Notbohm, J., Rosakis, A., Kumagai, S., Xia, S., and Ravichandran, G., 2013, "Three‐dimensional Displacement and Shape Measurement with a Diffraction‐assisted Grid Method," Strain.

[38] Badulescu, C., Grédiac, M., Mathias, J., and Roux, D., 2009, "A procedure for accurate one-dimensional strain measurement using the grid method," Experimental Mechanics, 49(6), pp. 841-854.

[39] Dupré, J.-C., Brémand, F., and Lagarde, A., 1993, "Numerical spectral analysis of a grid: Application to strain measurements," Optics and Lasers in Engineering, 18(3), pp. 159-172.

[40] Badulescu, C., Grédiac, M., and Mathias, J., 2009, "Investigation of the grid method for accurate in-plane strain measurement," Measurement Science and Technology, 20(9), p. 095102.

[41] Brown, D. C., " Decentering distortion of lenses," Photogrammetric Engineering, 32(4), pp. 444-462.

[42] Yoneyama, S., Kitagawa, A., Kitamura, K., and Kikuta, H., 2006, "In-plane displacement measurement using digital image correlation with lens distortion correction," JSME International Journal Series A, 49(3), pp. 458-467.

[43] Jin, H., and Bruck, H. A., 2005, "Pointwise digital image correlation using genetic algorithms," Experimental Techniques, 29(1), pp. 36-39.

[44] Réthoré, J., Hild, F., and Roux, S., 2008, "Extended digital image correlation with crack shape optimization," International Journal for Numerical Methods in Engineering, 73(2), pp. 248-272.

[45] Poissant, J., and Barthelat, F., 2010, "A novel “subset splitting” procedure for digital image correlation on discontinuous displacement fields," Experimental mechanics, 50(3), pp. 353-364.

[46] Liu, Y., and Fischer, G., 1997, "In situ measurement of local strain in a metal matrix composite by the object grating technique," Scripta materialia, 36(10), pp. 1187-1194.

[47] Balasubramanian, N., 1982, "Optical system for surface topography measurement," Google Patents.

[48] Sutton, M. A., Orteu, J. J., and Schreier, H., 2009, Image correlation for shape, motion and deformation measurements: basic concepts, theory and applications, Springer Science & Business Media.

[49] Jones, R., and Wykes, C., 1989, "Holographic and speckle interferometry," Holographic and Speckle Interferometry, by Robert Jones and Catherine Wykes, pp. 368. ISBN 0521348781. Cambridge, UK: Cambridge University Press, March 1989., 1.

[50] Li, L., and Yi, A. Y., 2010, "Design and fabrication of a freeform prism array for 3D microscopy," JOSA A, 27(12), pp. 2613-2620.

[51] Pan, Z., Xia, S., Gdoutou, A., and Ravichandran, G., 2014, "Diffraction-assisted image correlation for three-dimensional surface profiling," Experimental Mechanics, pp. 1-11.

[52] Arridge, S. R., 1999, "Optical tomography in medical imaging," Inverse problems, 15(2), p. R41.

[53] Gemmeke, H., and Ruiter, N., 2007, "3D ultrasound computer tomography for medical imaging," Nuclear Instruments and Methods in Physics Research Section A: Accelerators, Spectrometers, Detectors and Associated Equipment, 580(2), pp. 1057-1065.

[54] Sharpe, J., Ahlgren, U., Perry, P., Hill, B., Ross, A., Hecksher-Sørensen, J., Baldock, R., and Davidson, D., 2002, "Optical projection tomography as a tool for 3D microscopy and gene expression studies," Science, 296(5567), pp. 541-545.

[55] Elmoutaouakkil, A., Salvo, L., Maire, E., and Peix, G., 2002, "2D and 3D Characterization of Metal Foams Using X‐ray Tomography," Advanced engineering materials, 4(10), pp. 803-807.

[56] Maire, E., Colombo, P., Adrien, J., Babout, L., and Biasetto, L., 2007, "Characterization of the morphology of cellular ceramics by 3D image processing of X-ray tomography," Journal of the European Ceramic Society, 27(4), pp. 1973-1981.

[57] Uchic, M. D., Holzer, L., Inkson, B. J., Principe, E. L., and Munroe, P., 2007, "Three-dimensional microstructural characterization using focused ion beam tomography," MRS bulletin, 32(05), pp. 408-416.

[58] Williams, D. B., and Carter, C. B., 1996, The transmission electron microscope, Springer.

[59] Edelman, R. R., and Warach, S., 1993, "Magnetic resonance imaging," New England Journal of Medicine, 328(10), pp. 708-716.

[60] Xia, S., Pan, Z., and Zhang, J., 2014, "Optical microscope for three-dimensional surface displacement and shape measurements at the microscale," Optics letters, 39(14), pp. 4267-4270.

[61] Stephens, D. J., and Allan, V. J., 2003, "Light microscopy techniques for live cell imaging," Science, 300(5616), pp. 82-86.

[62] Ferraro, P., Grilli, S., Alfieri, D., De Nicola, S., Finizio, A., Pierattini, G., Javidi, B., Coppola, G., and Striano, V., 2005, "Extended focused image in microscopy by digital holography," Optics express, 13(18), pp. 6738-6749.

[63] Forster, B., Van De Ville, D., Berent, J., Sage, D., and Unser, M., 2004, "Complex wavelets for extended depth‐of‐field: A new method for the fusion of multichannel microscopy images," Microscopy Research and technique, 65(1‐2), pp. 33-42.

[64] Valdecasas, A. G., Marshall, D., Becerra, J. M., and Terrero, J., 2001, "On the extended depth of focus algorithms for bright field microscopy," Micron, 32(6), pp. 559-569.

[65] Fish, D., Brinicombe, A., Pike, E., and Walker, J., 1995, "Blind deconvolution by means of the Richardson–Lucy algorithm," JOSA A, 12(1), pp. 58-65.

[66] Prevedel, R., Yoon, Y.-G., Hoffmann, M., Pak, N., Wetzstein, G., Kato, S., Schrödel, T., Raskar, R., Zimmer, M., and Boyden, E. S., 2014, "Simultaneous whole-animal 3D imaging of neuronal activity using light-field microscopy," Nature methods.

[67] Vio, R., Bardsley, J., and Wamsteker, W., 2005, "Least-squares methods with Poissonian noise: Analysis and comparison with the Richardson-Lucy algorithm," Astronomy & Astrophysics, 436(2), pp. 741-755.

[68] Dey, N., Blanc‐Feraud, L., Zimmer, C., Roux, P., Kam, Z., Olivo‐Marin, J. C., and Zerubia, J., 2006, "Richardson–Lucy algorithm with total variation regularization for 3D confocal microscope deconvolution," Microscopy research and technique, 69(4), pp. 260-266.

[69] Bouguet, J.-Y., 2013, "Camera Calibration Toolbox for Matlab," http://www.vision.caltech.edu/bouguetj/calib_doc/.